CONSTRAINING THE SLIP RATE OF THE OWL LAKE FAULT BY USING LiDAR DATA AND FAULT SCARP DEGRADATION MODELS

A Thesis

Presented to

the Faculty of the Graduate School

at the University of Missouri - Columbia

In Partial Fulfillment

of the Requirements for the Degree

Master of Science

By

Gozde Altuntas

Assoc. Prof. Francisco Gomez, Thesis Supervisor

JULY 2022

The undersigned, appointed by the dean of the Graduate School, have examined the thesis entitled:

CONSTRAINING THE SLIP RATE OF THE OWL LAKE FAULT BY USING LiDAR DATA AND FAULT SCARP DEGRADATION MODELS

presented by Gozde Altuntas,

a candidate for the degree of Master of Science,

and hereby certify that, in their opinion, it is worthy of acceptance.

Dr. Francisco Gomez

Dr. Tandis Bidgoli

Dr. Neil Fox

ACKNOWLEDGEMENTS

First, I would like to thank the Turkish Ministry of National Education for the scholarship; this project would not have been possible without this opportunity.

I want to express my deepest gratitude to my research advisor, Francisco Gomez, for making this research feasible during the pandemic and for his guidance, support, and encouragement to complete my master's degree. Thanks to committee members Tandis Bidgoli and Neil Fox for their collaboration and feedback on my thesis. I am glad that I had the pleasure of working with them. Thanks should also go to Sean Polun for his role in the field and office work.

My heartfelt appreciation goes to my dear husband, Bolkar Altuntas, and my family as a whole for their love and care; for supporting me and my dreams. Even though being away from each other for 2.5 years was painful, I know they were always with me, and I am very grateful to have them in my life.

I am also thankful for having amazing friends in my life. Thanks to Hande Mahide Okutan, Cihan Okutan, and Mehmetcan Donmez for their friendship (since 2008), love, support, helping me on my maps, and sharing my stress; to Berk Duruturk for spending hours with video calls to motivate me and work together; to Utku Kocum for his help, advice, and support. Finally, special thanks go to my roommate, Mervegul Ozdas, for supporting, caring, sharing all the joy and stress, and being family to each other. We could not imagine those difficult, crazy times. I am thankful for everything you taught me.

I also thank the University of Missouri - the Department of Geological Sciences, the American Association of Petroleum Geologists (AAPG), the Geological Society of America (GSA), and the Association of Environmental & Engineering Geologists (AEG) foundations for research grants and funds.

TABLE OF CONTENTS

LIST OF FIGURES

LIST OF TABLES

CONSTRAINING THE SLIP RATE OF THE OWL LAKE FAULT BY USING LiDAR DATA AND FAULT SCARP DEGRADATION MODELS

Gozde Altuntas

Dr. Francisco Gomez Thesis Supervisor

ABSTRACT

The Owl Lake Fault is an active, 19 to 25-km-long, left-lateral strike-slip fault that divaricates NE from the Garlock Fault toward Death Valley in eastern California and transfers regional strain to the fault systems in Death Valley. As an active fault, the Owl Lake Fault is a poorly understood link between the extension of Death Valley and other active faults within Mojave Desert. In addition to the larger tectonic framework, improved understanding of the Owl Lake Fault as a seismogenic structure has direct implication for the assessment of the earthquake hazard in Eastern California. A significant limitation on the understanding of the Owl Lake Fault's role is the wide range of estimates previously reported for its slip rate. These range from 0.5 to 7.8 mm/yr, which implies the Owl Lake Fault may accommodate nearly all of the present-day slip on the Garlock Fault. The project aims to constrain the slip rate and understand kinematics of the Owl Lake Fault. For this project, I have used recent airborne LiDAR data (approximately 4.6 points/m^2) to map the fault and precisely measure horizontally offset landforms along the Owl Lake Fault. Subsequent to LiDAR mapping, field work facilitated the ground-truth verification of initial mapping as well as more precise measurements of small fault offsets using kinematic GPS and low-altitude photogrammetry. The detailed, local 'microtopography' permits assessing the smallest offsets (75-100 cm) which are interpreted as reflecting the last coseismic offset. Initial efforts at refining the slip rate use scarp degradation models to infer the ages of alluvial

fans and stream terraces that are offset by faulting. The final step for this project involves estimating slip rate, magnitude, and recurrence interval. Neotectonic investigations allowed to constrain the slip rate of the Owl Lake Fault as 1.1 - 1.4 mm/yr. The Owl Lake Fault can produce earthquake with the magnitude M=7.2 with the 1030 – 1430-yr recurrence interval. This study demonstrates that the Owl Lake Fault is part of the same hazard consideration as the central Garlock Fault in eastern California.

1. INTRODUCTION

Eastern California is an active, complex tectonic region including many faults with different kinematics. Deformation is broadly distributed in this region, and faults create a complicated tectonic puzzle. The Owl Lake Fault is a small, geometrically peculiar structure linking larger tectonic elements: the Garlock Fault, Eastern California Shear Zone, and the Basin-and-Range tectonic province. The Basin-and-Range and the right-lateral, Eastern California Shear Zone account for 30% of the relative motion of the Pacific and North American plates (e.g., Dokka and Travis, 1990; Dickinson and Wernicke, 1997). The left-lateral Garlock Fault also contributes to the regional strain, with a Late Quaternary slip rate of approximately 5-7 mm/yr (McGill et al., 2009; Ganev et al., 2012). The left-lateral Owl Lake Fault splays from the Garlock Fault as it strikes NE-SW with a length of 19-25 km (Figure 1-1).

This project aims to constrain the slip rate, earthquake behavior, and assess the regional kinematic role of the Owl Lake Fault. Prior work suggests that this left-lateral fault slips at 0.5-7.8 m/yr (McGill, 1999; Bryant, 2003). The broad range of the Owl Lake Fault's slip rate reported in the USGS Quaternary Fault Database (Bryant, 2003) allows for scenarios ranging from accommodating nearly all of the Garlock Fault's slip to a negligible amount. Constraining the slip rate on the Owl Lake Fault is key to understanding its role as a tectonic linkage between the Garlock Fault and Death Valley, as well as understanding how the Garlock Fault kinematics change along strike – the Owl Lake Fault may 'leak' slip from the western and central Garlock Fault as its strike changes eastward.

With a better understanding of neotectonics of the Owl Lake Fault in Eastern California, these hypotheses will be tested:

(1) Regional Kinematic significance

   A. The Owl Lake Fault transfers all the slip from the Garlock Fault to Death Valley: In this case, the slip rate of the Owl Lake Fault equals the slip rate of the western and central Garlock Fault

   B. Alternatively, some of the slip from the Garlock Fault transfers eastward to the Avawatz Mountains

(2) Earthquake Behavior

   A. The Owl Lake Fault ruptures as an independent, seismogenic structure: Rupture length of the Owl Lake Fault creates the measured average displacement

   B. The Owl Lake Fault ruptures along with part of the central Garlock Fault: Average displacement on the Owl Lake Fault is caused by rupture of the Owl Lake and the central Garlock Fault

This study assesses the Owl Lake Fault's slip rate and seismogenic behavior through the analysis of high-resolution topographic data (LiDAR, NAIP, and low-altitude photogrammetry) and new age constraints. In particular, airborne LiDAR data (approximately 4.6 points/m^2) enable detailed mapping of the Owl Lake Fault and measurement of multiple large offsets. Additionally, the Owl Lake Fault kinematics change from predominantly strike-slip in the SW to a combination of strike-slip and normal faulting in the NE, associated with along-strike changes in fault geometry.

Subsequent to LiDAR mapping, fieldwork facilitated the ground-truth verification of initial mapping as well as more precise measurements of small fault offsets using kinematic GPS and low-altitude photogrammetry. The detailed, local 'microtopography' permits assessing the smallest offsets (75-100 cm), which are interpreted as reflecting the last coseismic offset.

In addition to the larger tectonic framework, an improved understanding of the Owl Lake Fault as a seismogenic structure has direct implications for assessing the earthquake hazard in Eastern California. Improved estimates of slip rate and past earthquake magnitudes will help refine the understanding of the fault's potential future earthquakes, repetition, and possible effects because understanding fault behavior can inform strategies for probabilistic hazard characterization. In addition to that, this may also have implications for the earthquake potential of the eastern Garlock Fault. As past earthquakes have shown (e.g., Stein et al., 1997), including the recent 2019 earthquakes in Ridgecrest, CA, an earthquake on one fault can influence (increase or decrease likelihood) of earthquake occurrence on nearby faults.

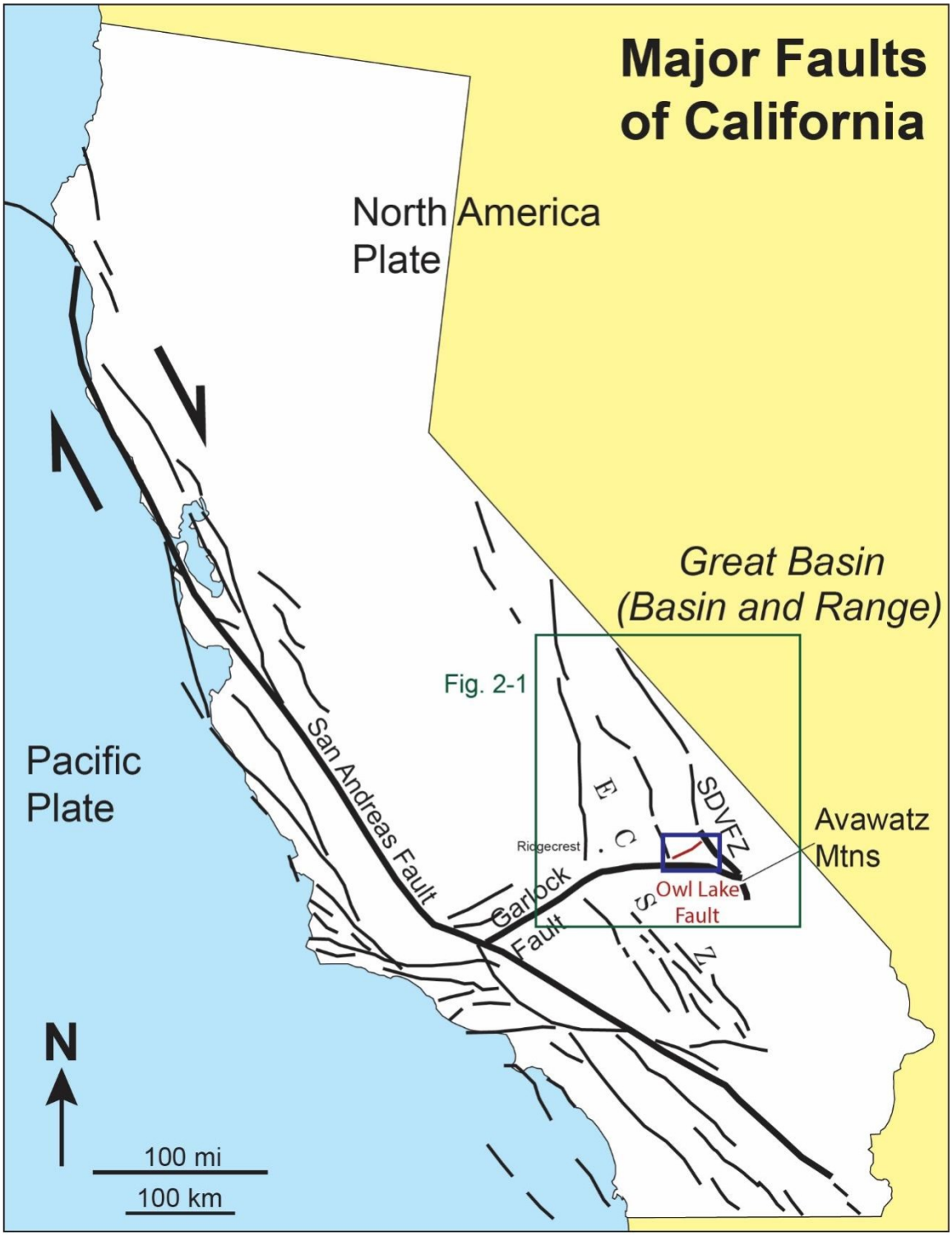

Figure 1-1. Location map showing major faults in California including Owl Lake Fault diverges from the Garlock Fault. SDVFZ: Southern Death Valley Fault Zone, ECSZ: Eastern California Shear Zone

Figure 1-2. The left-lateral Owl Lake Fault

2. GEOLOGIC SETTING

The Owl Lake Fault is located in the southeastern Owlshead Mountains of eastern California (Figure 1-1). The study area has an elevation of 600 to 1200 meters. The climate of the Owl Lake Fault, as well as the greater Death Valley basin area is classified as hot desert (Koppen classification BWH). Owl Lake receives an average annual rain fall of 80-90 mm/year (based on nearby data from Fort Irwin and Baker; https://www.usclimatedata.com). As part of the complex structure of Eastern California, the Owl Lake Fault is a piece of the puzzle linking the Garlock Fault, Eastern California Shear Zone, and the Basin-and-Range tectonic province (Figure 1-1).

2.1. Tectonic Elements

2.1.1. Eastern California Shear Zone

The Eastern California Shear Zone (ECSZ), identified by Dokka and Travis (1990a, 1990b), accommodates almost 25% of the motion between North America and Pacific plates (Liu, et al., 2010). The shear zone acts differently between the north and south of the Garlock Fault. South of the Garlock Fault, the ESCZ consists of many dextral active strike-slip faults, including Helendale Fault (HF), Lenwood Fault (LF), Camp Rock Fault (CRF), Calico Fault (CF), Pisgah Fault (PF), and Ludlow Fault (LuF) - from west to east. North of the Garlock Fault, there are three transtensional fault zones that are part of the western Basin-and-Range Province: (1) the Owens Valley, Airport Lake Fault Zone, (2) the Panamint Valley, Hunter Mountain, Saline Valley Fault Zone, and (3) the Death Valley, Furnace Creek, Fish Lake Fault Zone (Dixon and Xie, 2018).

The ECSZ started forming approximately between 12 and 5 Ma when the Gulf of California began to form due to the migration of the North America and Pacific plate boundary (Plattner, 2010; Dixon and Xie, 2018). This opening caused the slip of the southern San Andreas Fault to jump inland (Oskin and Stock, 2003) and as a result of the formation of the Big Bend (Dixon and Xie, 2018; Liu et al., 2010). This formation transferred some crustal strain inland along the ECSZ (Liu et al., 2010). Considering that the northern Gulf of California had opened as a marine basin by approximately 6.2 ± 0.2 mya (Bennett et al., 2015), the ECSZ might be formed around 6-8 mya. Basin and Range extension and the Garlock Fault also developed the ECSZ (Liu et al., 2010). The ECSZ also had an impact on the change of motion of the Sierra Nevada block from westward during Late Miocene to northwesterly direction in present (Dixon and Xie, 2018). The ECSZ, as well as deformation in the western Basin and Range, may have accelerated in response to crustal delamination of the southern Sierra Nevada, as well (e.g., Gourmelen et al., 2011).

2.1.2. Basin and Range

The Basin and Range Province is a wide extensional terrane that formed from Canada through western North America and the northern part of Mexico (Parsons, 2006). Whereas the central Basin and Range initiated between late Oligocene and Early Miocene (Wernicke, 1992), the northern and southern Basin and Range experienced broad extension in Middle Miocene (~13-10 Ma) (Parson, 2006). Basin and Range extension produced north-northeast trending basins and ranges in a region several-hundred-km-wide (Parsons, 2006; Camp et al., 2015). The Owl Lake Fault lies between the Panamint Valley and Death Valley in southwestern Basin and Range.

2.1.3. Garlock Fault

The Garlock Fault is a major, left-lateral strike-slip fault in southern California. The fault intersects with the San Andreas Fault on its western edge, strikes northeast and bends ~15° to the east, and finally changes its strike to the southeast at the end of the fault in the Avawatz Mountains. The fault separates the Basin and Range Province and the Sierra Nevada from the northern Mojave Desert. The total length of the fault is approximately 270 km, and 48 to 64 km of left-lateral displacement was measured and documented by many authors (Davis and Burchfiel, 1973; McGill, 1992; McGill and Sieh, 1993).

The initial movement of the left-lateral Garlock Fault dates back to Middle-Late Miocene (~17-10 Ma) (Burbank and Whistler,1987; Monastero, 1997, Andrew et al., 2014). The initiation of the Garlock Fault has been explained by three possible tectonic models (Figure 2-2). The first model suggests the Garlock Fault, Big Pine Fault, and the San Andreas Fault are conjugate faults as a part of the regional strain (Hill and Dibblee, 1953; McGill, 2009). The second model proposed by Davis and Burchfiel (1973) suggests that the Garlock Fault is a transform structure between the Basin and Range and the Mojave block. The third model proposes that the initiation of the Garlock Fault is related to the rotation of the Mojave block (Guest et al., 2003).

The Garlock Fault is generally divided into three segments (McGill and Sieh, 1991; McGill, 1992): (1) a western segment from the intersection with the San Andreas Fault to Koehn Lake region, (2) a central section from the ~2-km left stepover at the Koehn Lake to the Quail Mountains where it intersects the Owl Lake Fault, and (3) an eastern segment from Quail Mountains to the intersection with the Southern Death Valley

Fault. Along these segments, the strike of the Garlock Fault changes from NE-SW in the west to E-W along the central and eastern sections and ESE-WNW as it terminates in the Avawatz Mountains (Figure 2-3).

Davis and Burchfiel (1973) suggested two possible structural configurations for the eastern Garlock Fault: (1) the eastern Garlock Fault terminates at the southern Death Valley Fault Zone (SDVFZ) and Avawatz Mountains, or (2) the eastern Garlock Fault extends through Kingston Wash with the same trend. The hypothesis for possible extension of the Garlock Fault beneath the Kingston Wash was tested by Plescia and Henyey (1982) by geophysical investigations consisting of gravity and magnetic surveys and corroborated with geologic data. These surveys inferred lineaments beneath the Kingston Wash (east of the SDVFZ) as the proposed extension of the Garlock Fault with a length of about 25-30 km (Plescia and Henyey, 1982).

2.2. Active Regional Deformation

Considering that the motion between the Pacific and North America plates has been constant during the Late Tertiary (Atwater, 1970), the motion of the Eastern California Shear Zone (ECSZ) may also be considered steady and accommodates dextral shear with the rate of 10-12 mm/yr (Dixon and Xie, 2018). The ECSZ expresses two different tectonic styles on the north and south of the Garlock Fault. North of the Garlock Fault, there are transtensional fault zones; on the other hand, dextral strike-slip faults comprised the ECSZ on the south of the Garlock Fault.

According to tectonic models for southern California, the western Mojave first rotated 35-45° clockwise and afterward was rotated with a compensable degree of 10–20.

The final rotation was obtained from the rocks as 25° clockwise (Golombek and Brown, 1988). These two opposite rotations were forced by the dextral shear of the western margin of North America ~20-5 Ma.

The Owlshead Mountains' reconstruction model by Guest et al. (2003) explains that the rotation of the Northeast Mojave block and the extension in the Basin and Range resulted in the transtension and rotation of the Owlshead Mountains. This movement of the Northeast Mojave Block also has an impact on the rotating of the eastern Garlock Fault around ~23-45° clockwise (Schermer et al., 1996; Guest et al., 2003). This misorientation of the eastern Garlock Fault caused this part to be incapable to accommodate the sinistral shear and transferred to the Owl Lake Fault and the Wingate Wash Fault Zones (Guest et al., 2003). The Garlock Fault has a Holocene – Late Pleistocene slip rate of approximately 5 – 7 mm/yr, and this rate decreases eastward (McGill, 1992; McGill et al., 2009; Ganev et al., 2012). Even though the Garlock Fault was active during the same period with the ECSZ, there is no evidence that the Garlock Fault was offset by ECSZ faults (Frankel et al., 2010; Dixon and Xie, 2018).

2.2.1. Present Day Movement

Zeng and Shen (2016) developed a fault-based model by inverting GPS velocity data to provide slip rate estimates for California (Figure 2-4). In this study, geologic and geodetic slip rates were compiled and combined with new data. Mostly, these two estimates were well correlated; however, there are some discrepancies for some faults. For instance, the inverted slip rate and geologic slip rate match well. On the other hand, the inverted slip rate for the central Garlock Fault appears as significantly low (1.7 mm/yr). The other difference that the model shows is that the ECSZ has higher slip rate

than geologic slip rate. Zeng and Shen (2016) also suggested a slip rate of the Owl Lake Fault as 2.27±0.46 mm/yr based on modeling GPS observations of crustal deformation as elastic blocks bounded by faults.

2.2.2. Seismicity

The seismicity along the Garlock Fault is different on the western and eastern parts of the fault. Seismological studies on the Garlock Fault show that the eastern part of the fault produces less activity and fewer earthquakes; on the other hand, the western part of the fault produces continuous and numerous low magnitude earthquakes (Astiz and Allen, 1983; Petersen and Wesnousky, 1994). Additionally, the aseismic creep has been observed on the western segment (westernmost ~60km) of the Garlock Fault (McGill, 1992).

Eastern California as a one of the most seismically active regions in western North America has witnessed numerous moderate and large earthquakes. Recent large earthquakes in the region are M=7.3 Landers Earthquake in 1992, M=7.1 Hector Mine Earthquake in 1999, and the 2019 Ridgecrest earthquakes (M=6.4 on July 4th and M=7.1 on July 6th) (Figure 2-5).

Although there are no recorded historical earthquakes on the Garlock Fault, two moderate earthquakes occurred in 1916 near the fault, creating the possibility that the Garlock Fault could be the source of these earthquakes. The first event on October 23 was reported as M=5.2 at the western end of the Garlock Fault; however, possible sources for this earthquake might be the San Andreas and the neighboring faults (McGill and Sieh, 1991; McGill, 1992). The second event on November 10 was reported as M=6.1 at

~40 km east of the eastern Garlock Fault in 1965 and M=5.5 at ~45 km north of the Garlock Fault in the vicinity of Quail Mountains in 1978. The suspicion that the source of the earthquake might be the Garlock Fault or the Owl Lake Fault remains gripping since the exact location of the earthquake has not been determined (McGill and Sieh, 1991; McGill, 1992).

Figure 2-5 shows the seismic activity of the area that is closest to the Owl Lake Fault from the 1960 to present with recent earthquakes in the vicinity. Although there are no instrumentally recorded earthquakes documented on the Owl Lake Fault, the offsets on this fault are proof of prehistoric earthquakes.

2.3. The Owl Lake Fault

The Owl Lake Fault is an approximately 19-25 km-long, left-lateral, oblique-slip normal fault in Eastern California. The fault was initially mapped by Muehlberger (1954). While mapping the 7 km southwest of the fault, he defined the fault as a reverse fault and added that the fault became a normal fault further to the northeast. When Clark (1973) mapped the recent movements of the Garlock Fault and the Owl Lake Fault, he identified channels and ridges with left-lateral offsets to the southwest of the Owl Lake Fault; however, he did not observe any recent lateral displacement on the northeast part of the fault.

The Owl Lake Fault may have initiated as a tectonic response with the rotation of the Garlock Fault (e.g., Guest et al., 2003). As the strike of the Garlock Fault changes eastward, the left-lateral slip of the Garlock Fault was probably transferred at which Garlock Fault intersects the Owl Lake Fault to the eastern Garlock Fault and the Owl

Lake Fault (McGill, 1998). This may decrease the slip rate of the eastern Garlock Fault. In addition to this, the Mule Springs strand probably became inactive because of this transferred left-lateral slip from the Garlock Fault to the Owl Lake Fault (Guest et al., 2003).

As an active fault at the present time, the Owl Lake Fault is a poorly understood tectonic linkage between the extension of Death Valley and other active faults within the Mojave Desert. The fault intersects with the Garlock Fault and the Brown Mountains in the Quail Mountains and extends toward to Owlshead Mountains. This region shows both rotation and transtension in consequence of the clockwise rotation of the Northeast Mojave block and the extension of Basin and Range Province (Guest et al., 2003).

2.3.1. General Geology along the Owl Lake Fault

The Owl Lake Fault diverges from the Garlock Fault in Quail Mountains and lies northeasterly through the Owlshead Mountains. According to the "Generalized Surficial Geologic Mapping of the Fort Irwin Area" map and report by Miller et al., 2014, the geology of the Owl Lake Fault mainly is composed of Miocene volcanic rocks (mv), late to middle Pleistocene alluvial fan deposits (Qia), and latest Pleistocene to Holocene alluvial fans (Qya, Figure 2-6). Near the intersection of the Owl Lake Fault and Garlock Fault, Mesozoic plutonic rocks (fpg) and Miocene sedimentary rocks (pc) are exposed. Besides, the northeastern Owl Lake Fault was not mapped by Miller. Considering that the fault extends to the Owlshead Mountains, the geological units of this part of the fault can be referred from this region's geology. The Owlshead Mountains consist of Mesozoic volcanic and metamorphic rocks (Davis, 1982; Guest et al., 2003), and Tertiary and Quaternary volcanic rocks overlie these units (Davis, 1982; Guest et al., 2003). This

information is consistent with the observed rocks such as granites and marbles in the study area.

2.3.2. Prior Neotectonic Studies

Recent fault breaks in the Owl Lake Fault were observed to be younger than fault breaks in the 13-km-long strand of the Garlock Fault, which strengthens the prospect that the recent rupture in the Pilot Knob Valley section of the Garlock Fault continued towards the Owl Lake Fault rather than continuing east of the Garlock Fault (Clark, written comm., 1990; McGill, 1992). In addition to this, the fact that the recent fault breaks in the southwest of the Owl Lake Fault are closer to the recent fault breaks in the east of the Garlock Fault (Clark, 1973) supports that the Owl Lake Fault is a part of the Garlock Fault (McGill and Sieh, 1991; McGill, 1992).

McGill and Sieh (1991) present numerous rupture patterns for the Garlock Fault, considering that the fault ruptured entirely in a single event (Mw = 7.8) or shorter segments in multiple events (ranges from Mw = 6.6 to Mw = 7.5). In these patterns, two assumptions were made for the Owl Lake Fault with the lack of information about slip amount and left-lateral offset on the northeastern part of the Owl Lake Fault. The first rupture pattern shows the rupture from the central Garlock Fault to the Owl Lake Fault and second pattern shows the rupture of the Owl Lake Fault itself. According to these patterns, the possible earthquake magnitudes were calculated by applying Wells and Coppersmith (1994) empirical relationship as M = 7.5 and M = 6.6, respectively (Figure 2-7).

McGill (1998) estimated the slip rate of the Owl Lake Fault on a terrace riser at the southeast end of the fault, in a region close to the intersection of the Owl Lake Fault with the Garlock Fault. Since the intersection of the top of the terrace with the Owl Lake Fault is covered by colluvium, the difficulty in determining the location of the piercing point presented a wide range from 19 m to 235 m lateral and from 2 to 28 m vertical displacements.

The age of the alluvial deposit was determined as 30,820 BP and 29,490 BP by using AMS radiometric dating on organic materials obtained from two of the six boulders. Thus, the slip rate estimations for 19 to 235 m left-lateral, and 2 to 28 vertical displacements were calculated as 0.5 to 7.8 mm/yr and 0.06 to 0.9 mm/yr, respectively (McGill, 1998a, 1998b). The Owl Lake Fault's preferred left-lateral slip rate was calculated as 2.5 mm/yr for 80-m-displacement in 31.5 kyr (McGill 1993, 1998a, 1998b).

One concern with this slip rate estimate pertains to the dating method used: radiocarbon dating of organic material contained within rock varnish. As discussed by Dorn (1996), who had previously performed the dating for McGill (1993), two potential problems with this method are now recognized: (1) It is not open system, that causes the exchange in the system; and (2) Invasion of the different materials can result in different ages within the same sample. Therefore, the slip rate derived from this age may not be reliable, and an alternative estimate of the faulted surface is required.

A significant limitation on the understanding of the Owl Lake Fault's role in this regional tectonic framework is the wide range of estimates on its slip rates which range from 0.5 to 7.8 mm/yr. This study aims to constrain the slip rate of the Owl Lake Fault to

contribute better understanding the fault's kinematics and future earthquake potential and provide key information on this tectonic linkage between the Garlock Fault and Death Valley.

Table 2-1. Rupture pattern with fault segments for the central Garlock Fault and the Owl Lake Fault. Modified from McGill and Sieh, 1991; McGill, 1992. OLF; Owl Lake Fault

Fault Segments	Rupture Length (km)	Magnitude (Mw)
Central Garlock Fault and Owl Lake Fault		
Cantil to Trona Rd	39	7.5
Trona Road to Quail Mts	66	
SW half of the OLF	11	
NE half of the OLF	8	
Owl Lake Fault		
Owl Lake Fault	19	6.6

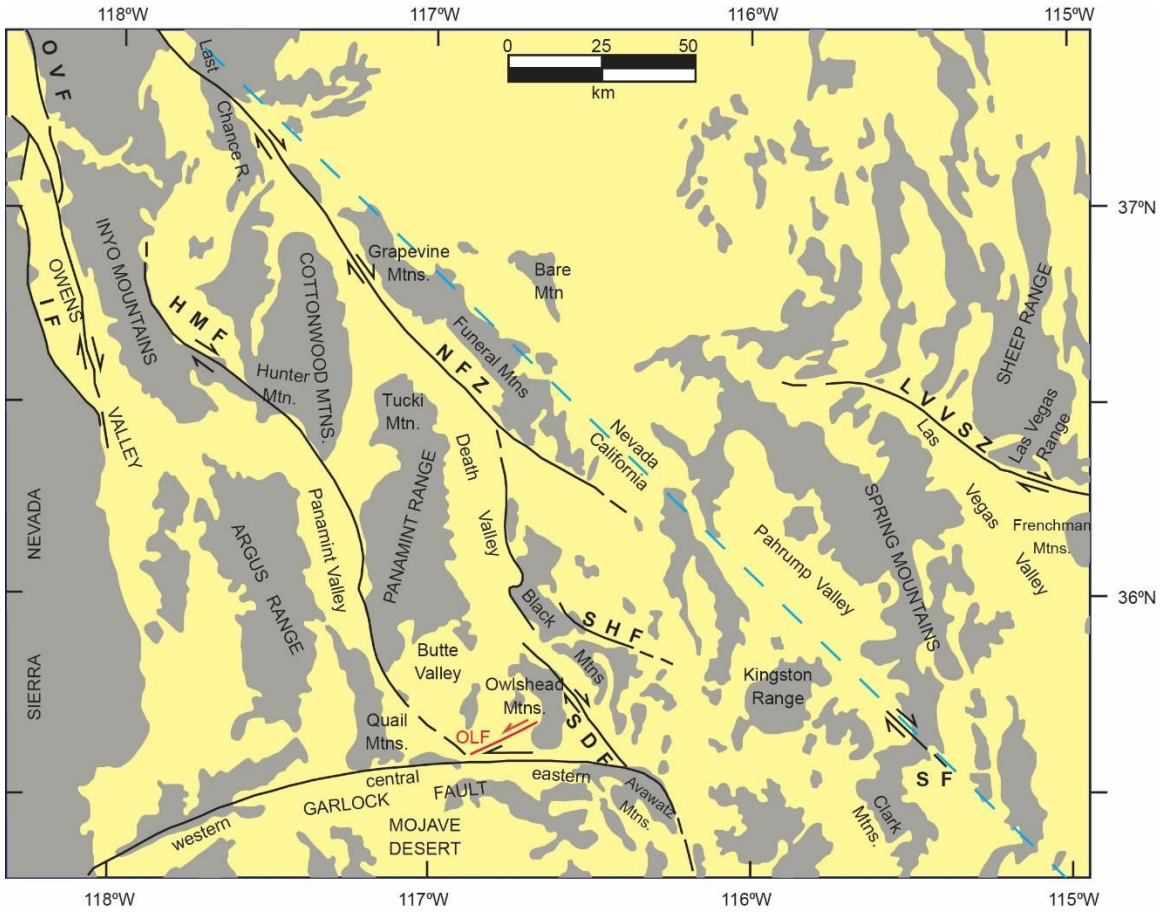

Figure 2-1. Simplified tectonic map of the region with Cenozoic fault zones. IF, Independence Fault; NFZ, Northern Death Valley-Furnace Creek Fault Zone; OLF, Owl Lake Fault; OVF, Owens Valley Fault; SDF, Southern Death Valley Fault, SF, State Line Fault, SHF, Sheep Head Fault. Modified from Wernicke et al, 1988.

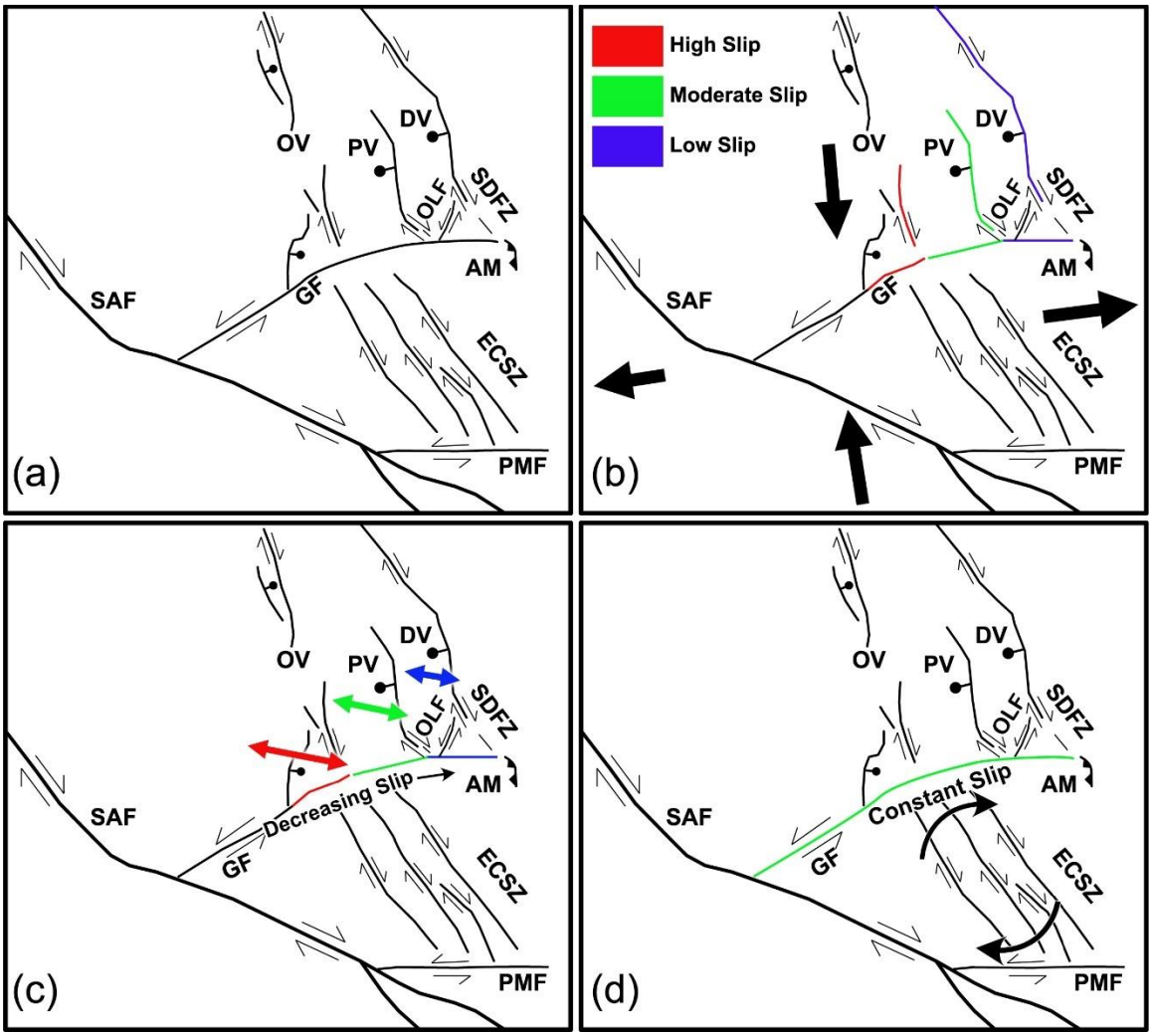

Figure 2-2. Possible tectonic models for the Garlock Fault. SAF: San Andreas Fault; GF: Garlock Fault; OV: Owens Valley; PV: Panamint Valley; DV: Death Valley; OLF: Owl Lake Fault; SDFZ: Southern Death Valley Fault Zone; AM: Avawatz Mountains; ECSZ: Eastern California Shear Zone; PMF: Pinto Mountain Fault. Modified from Polun et al., 2021.

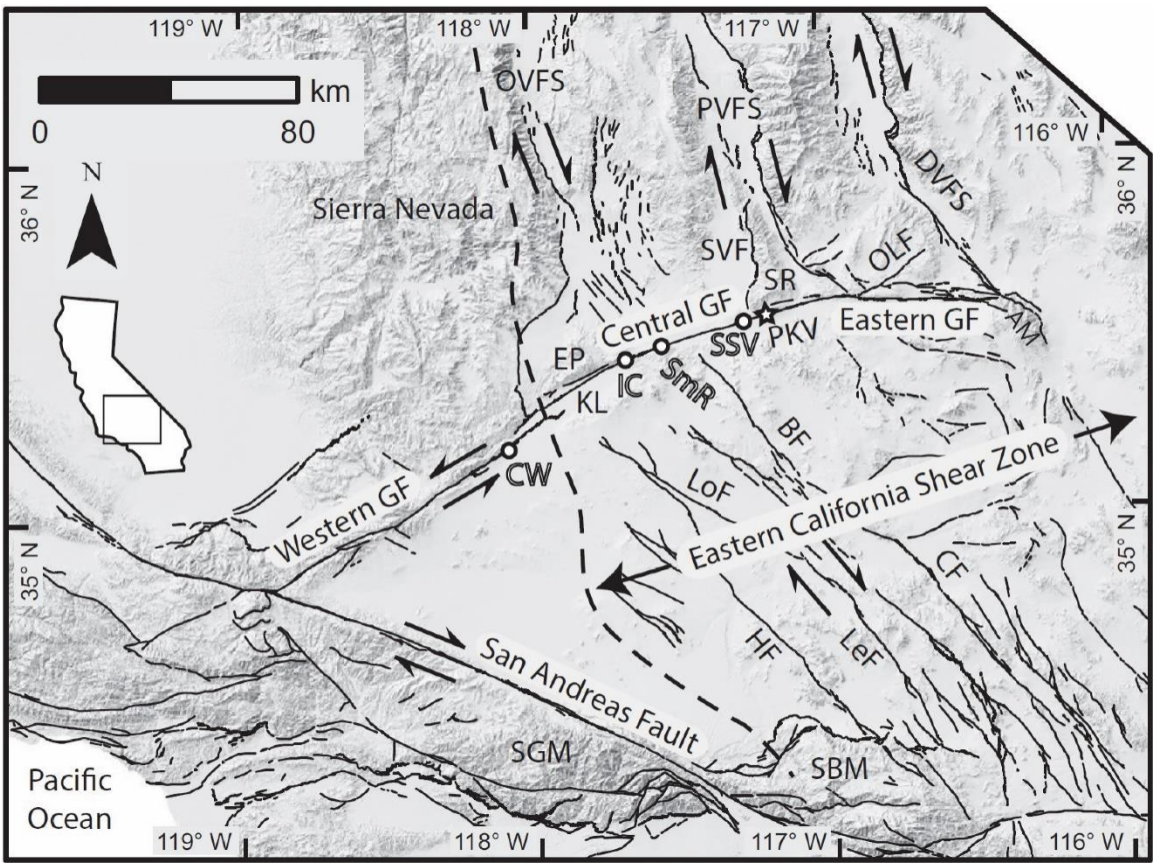

Figure 2-3. Segments of the Garlock Fault and Eastern California Shear Zone. Modified from Rittase et al., 2014. GF: Garlock Fault; OVSF: Owens Valley Fault System; PVSF: Panamint Valley Fault System; DVFS: Death Valley Fault System; CW: Clark Wash; IC: Iron Canyon; SmR: Summit Range; SSV: Southeast Searles Valley; BF: Blackwater Fault; CF: Calico Fault; EP: El Paso Mountains; HF: Helendale Fault; KL: Koehn Lake; LeF: Lenwood fault; LoF: Lockhart Fault; OLF: Owl Lake Fault; PKV: Pilot Knob Valley; SBM: San Bernardino Mountains; SGM: San Gabriel Mountains; SR: Slate Range; SVF: Searles Valley Fault. Dashed line: western edge of the Eastern California Shear Zone.

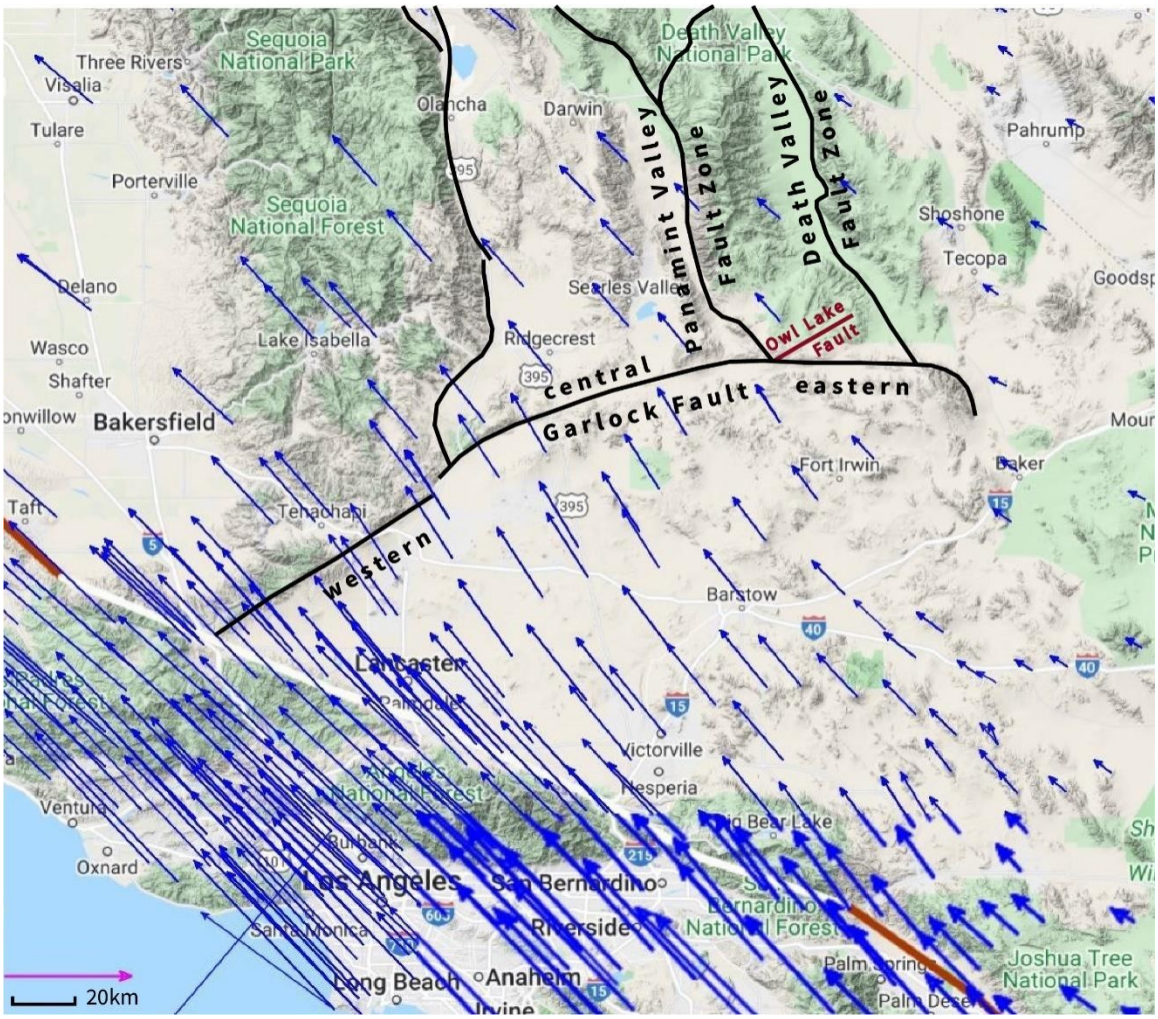

Figure 2-4. Global Positioning System (GPS) velocities for study area with major faults. https://www.unavco.org/software/visualization/GPS-Velocity-Viewer/GPS-Velocity-Viewer.html. GNSS data source: N. America, NAM14, UNAVCO.

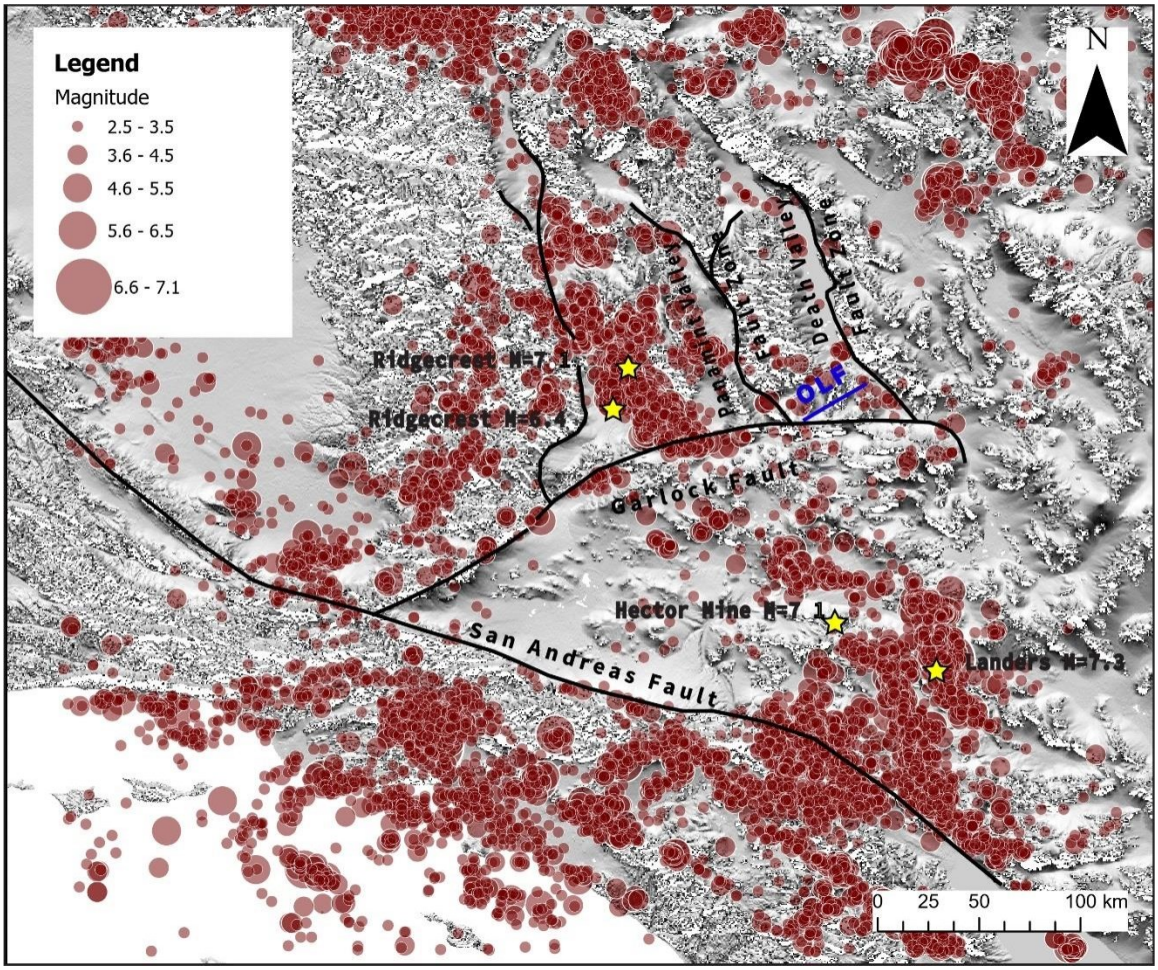

Figure 2-5. Seismicity map of the southeastern California. Earthquakes between 1960 and 2022 from USGS Earthquake Catalog. Stars show recent earthquakes – 1992 Landers, 1999 Hector Mine, and 2019 Ridgecrest Earthquakes. OLF: Owl Lake Fault

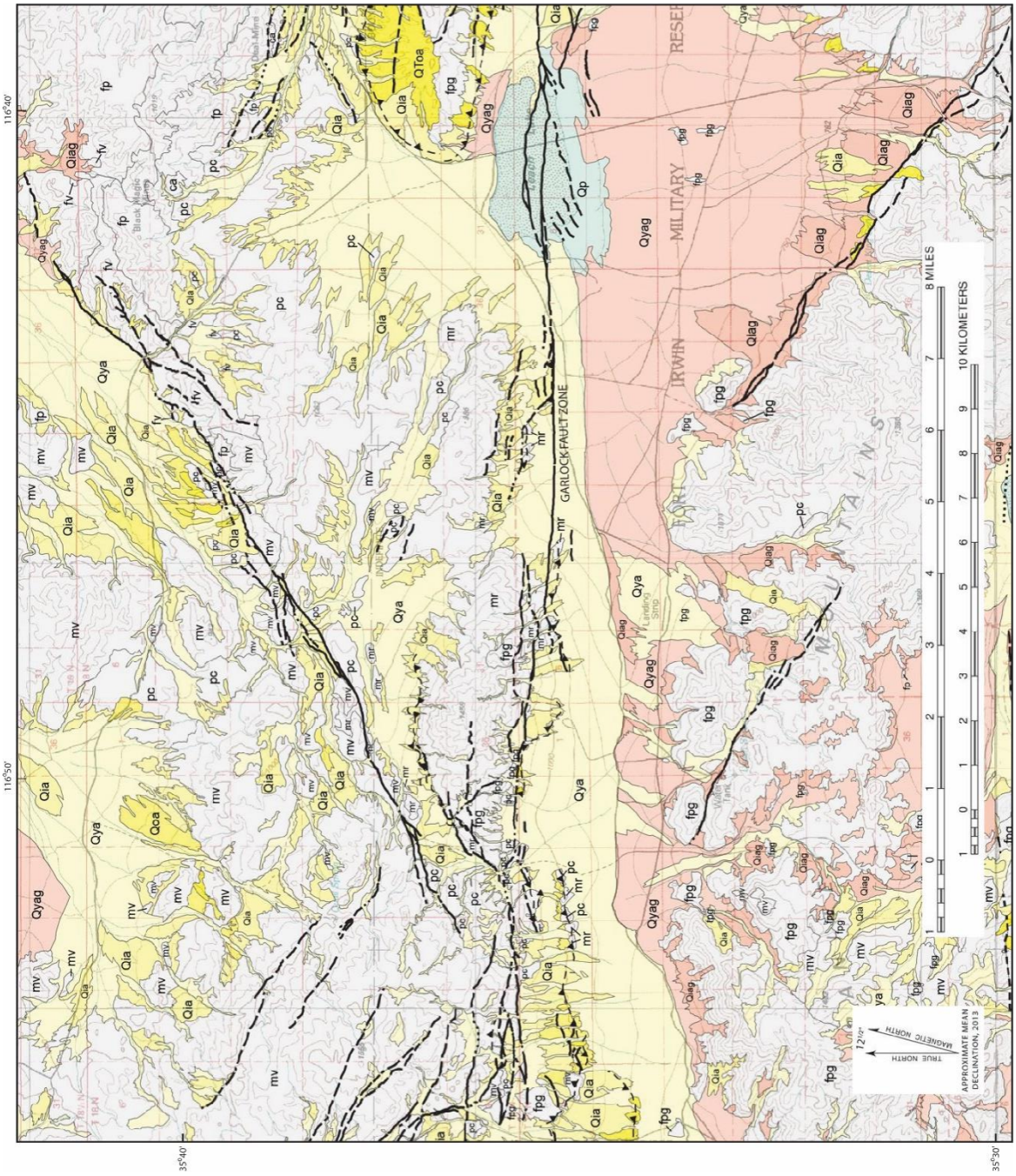

Figure 2-6. Surficial Geologic Map of the Owl Lake Fault. Modified from "Generalized Surficial Geologic Map of the Fort Irwin Area, San Bernardino County, California, Miller et al., 2014

MAP UNITS

SURFICIAL DEPOSITS

ANTHROPOGENIC DEPOSITS

ml **Made land (Holocene)**

ALLUVIAL FAN DEPOSITS

Qya **Young alluvial fan deposit (Holocene and latest Pleistocene)**

Qyag **Young alluvial fan deposit composed of grus**

Qia **Intermediate alluvial fan deposit (late to middle Pleistocene)**

Qiag **Intermediate alluvial fan deposit composed of grus**

Qoa **Old alluvial fan deposit (middle to early Pleistocene)**

QToa **Extremely old alluvial fan deposit (early Pleistocene to Pliocene)**

OTHER SURFICIAL DEPOSITS

Qe **Eolian sand deposit (Holocene and Pleistocene)**

Qp **Playa deposit (Holocene)**

Qg **Groundwater-discharge deposit (Holocene and Pleistocene)**

Ql **Lacustrine deposit (Holocene and Pleistocene)**

SUBSTRATE MATERIALS

Buried rock and partly consolidated materials that underlie pediment and hillslope veneers. Ages range from Pliocene to Proterozoic. Substrate materials are subdivided based on weathering characteristics and erosional products:

ca **Carbonate rocks**

fp **Felsic plutonic rocks**

fpg **Felsic plutonic rocks that weather to grus**

fv **Felsic volcanic rocks**

mp **Mafic plutonic rocks**

mv **Mafic volcanic rocks**

mr **Metamorphic rocks**

pc **Partly consolidated materials**

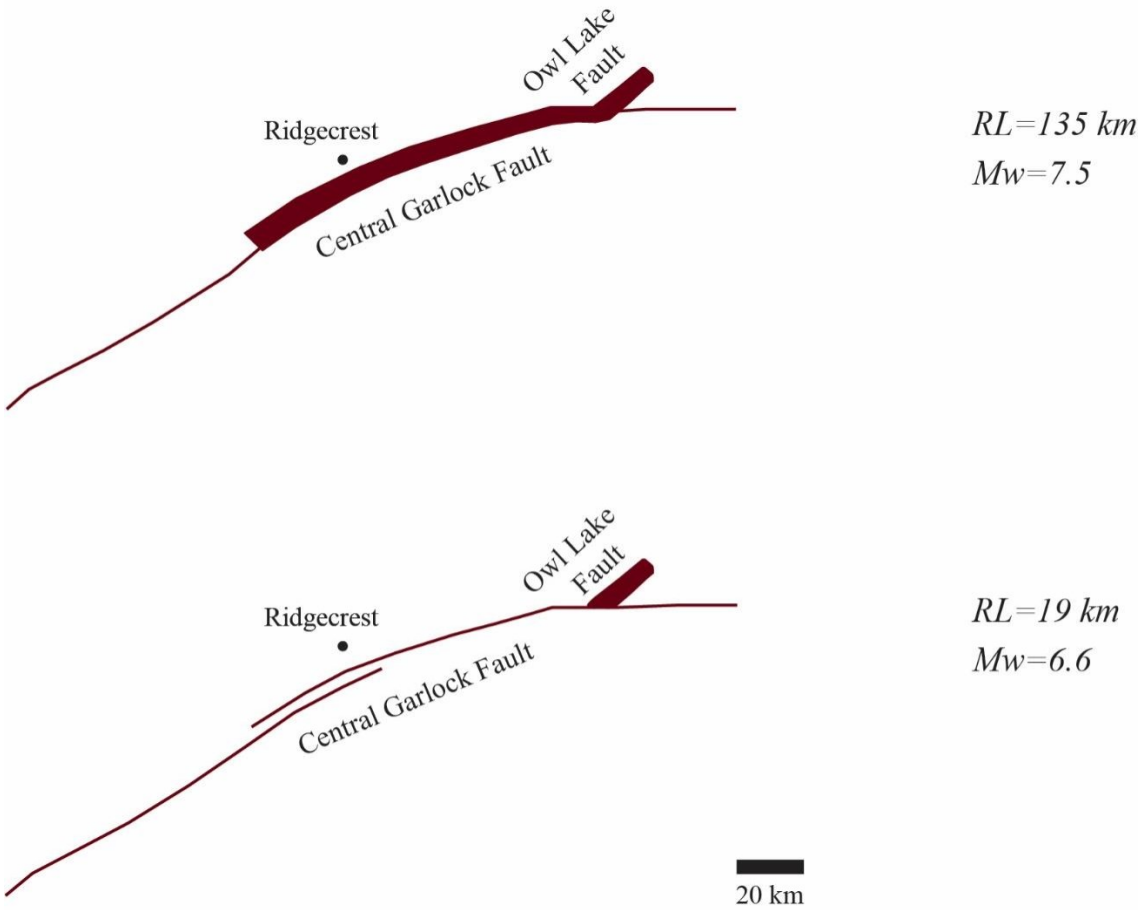

Figure 2-7. Possible rupture patterns for the Owl Lake Fault. Modified from McGill and Sieh, 1991; McGill, 1992. Magnitudes were calculated using Wells and Coppersmith (1994) empirical relationship for strike-slip faults

3. METHODS

In order to assess the slip rate and seismogenic behavior of the Owl Lake Fault this study uses high-resolution topography and imagery (LiDAR, NAIP, and low-altitude photogrammetry), and fault scarp analysis. In addition to the remote-sensing-based analysis, field work facilitated the ground-truth verification of initial mapping as well as more precise measurements of small fault offsets using kinematic GPS and other surveying methods.

3.1. Fault Mapping with LiDAR and Aerial Imagery

LiDAR (Light Detection and Ranging) is a modern tool for topographic mapping. LiDAR uses light as a pulsed laser to provide three-dimensional, high-resolution topography information of the Earth's surface. During the LiDAR surveying, a pulsed laser is emitted and the time-of-flight of the reflection (a.k.a., the "return") provides a precise measure of the distance from the aircraft. Accounting for the aircraft position and orientation, this becomes a measurement of the reflection point in 3-dimensional space. Importantly, the laser pulse may have multiple reflections - for example, earlier returns from the upper leaves or branches of vegetation and a last return from the bare ground. This ability to resolve bare ground reflections in vegetated regions is a powerful and advantageous capability of LiDAR, compared with other imaging methods (e.g., photogrammetry).

LiDAR data for this study are available from OpenTopography (https://www.opentopography.org). The specific data set was acquired in April 2007 as a part of "The EarthScope Southern & Eastern California Lidar Project" within the scope

of the EarthScope Project by NCALM (National Center for Airborne Laser Mapping) (Figure 3-1). The LiDAR data have an approximate point density of 4.6 points/m^2 and were already classified into bare ground points and non-ground points by Open Topography. Bare-earth LiDAR points were extracted from the point cloud and used to construct a 50-cm pixel digital elevation model (DEM). It should be remembered that some bare-ground points may represent large boulders, as well as incorrectly classified vegetation – from comparison with aerial imagery, these appear to be large boulders in most cases.

Besides LiDAR, the other aerial imagery used in this study is from the National Agriculture Imagery Program (NAIP), acquired by the US Department of Agriculture. NAIP is 4-band imagery (visible RGB + near infrared) that covers 3.75-minute by 3.75-minute latitude and longitude and has a resolution of 0.6 m ground sample distance (GSD). The NAIP images covering the study area were obtained from Earth Explorer, USGS (https://earthexplorer.usgs.gov). These images were acquired on the 23rd of May 2020.

Faults will often correspond with linear features (i.e., “lineaments”) in topography and image data, although it should be noted that inactive faults, tectonic fractures, and other geological features can also have quasi-linear expressions (e.g., Drury, 2004). Owing to the near vertical dip of most strike-slip faults (such as the Owl Lake Fault), topographic lineaments tend to be very straight (Yeats et al., 1996) (Figure 3-2). Interpreting a physiographic lineament as a fault is supported by other contextual features including (Keller & Pinter, 2002; Yeats et al., 1996):

- Abrupt changes in local topography – such convexities are termed “scarps” (“fault scarps”, when they form by fault displacement);
- Co-linearity and continuity of lineaments;
- Consistent direction of deflection of drainage patterns (larger deflections should correspond with larger and older drainages);
- Linear depressions (a.k.a., “sag depressions”);
- Alignment of springs and vegetation (particularly noticeable in arid regions);
- Abrupt terminations of ridges and other apparently offset landforms.

To help identify tectonic features, shaded relief images were made from the DEM, which allow for illuminating the bare ground surface from different sun angles. The advantage of changing the sun angle is that topographic lineaments are often more apparent when they create shadows with the low sun angle. Topographic lineaments also stand out when the azimuth of illumination is perpendicular to the feature. The ERMapper image processing software was used to construct these false-sun-shading relief images.

All imagery (LiDAR-derived and NAIP) were ingested into ArcGIS Pro to construct the fault map. In much of the area, the fault lineaments are very well expressed as they cut across alluvial fans and other landforms, although confident interpretation of offset features (i.e., “piercing points”) is restricted to specific locations.

3.2. Fault Scarp Analysis

Fault scarp morphology is another practical dating method within the context of Quaternary geochronology (Hanks, 2000). The aim of the application of this study is to estimate the approximate ages of faulted surfaces. This will provide critical information on timing to constrain rates of faulting.

Fault scarps are steep, straight slopes that have a height range from a few meters to hundreds of meters caused by tectonic offset of the earth's surface. In addition to total offset, false scarps may contain records of past earthquakes, such as recurrence intervals and faulting periods (Arrowsmith et al., 1998). Analysis of a degraded fault scarp contributes to estimating the time of the earthquake that causes the scarp and so uplift rate (Hanks et al., 1984; Hanks, 2000). This method does not include stratigraphic considerations like many methods and depends on simple geomorphic observations (Hanks, 2000).

Classically, fault scarps have been measured using field surveying (Hanks, 2000), but LiDAR point data (bare-earth points) are comparably dense spatially. Therefore, profiles are extracted from LiDAR. Locating the representative profiles for degradation modeling along the interested fault is based on two bases. First, profiles should be perpendicular to the fault scarp, and second, profiles should be located by avoiding upslope channels, gullies, and downslope fans (Hanks et al., 1984).

There are two primary assumptions for scarp degradation analysis; (1) mass conservation, and (2) mass (sediment) transportation in proportion to the topographic gradient (Hanks et al., 1984). These two assumptions result in a diffusion equation taking

into consideration that sediment transportation from higher elevation to lower elevation by gravity is a kind of diffusion process (Figure 3-3). This equation is identical to the differential equation for one-dimensional heat flow:

$$\frac{\partial u}{\partial t} - \kappa \frac{\partial^2 u}{\partial x^2} = 0 \quad (1)$$

where κ (Kappa) is mass diffusivity (m^2/ka) that varies depending on the geologic and climatic conditions; u represents the relative elevation as a function of both time, t, and distance, x. Equation (1) indicates the proportionality of the elevation change to the curvature of the slope. In other words, when the topography has a positive curvature (concave upward), elevation increases with time (depositional basins); conversely, when the topography has a negative curvature (concave downward), elevation decreases with time (ridge crests) (Hanks et al., 1984; Hanks, 2000). Additionally, equation (1) states that sharper topography degrades faster than smoother topography with the same constant κ (Hanks et al., 1984; Hanks, 2000, Figure 3-4). The value of κ may be regionally calibrated based on the research area's climatic conditions (Hanks et al., 1984).

Considering that faulting events for fault scarps might be episodic with the slip rate of 2A, equation (1) turns into,

$$\frac{\partial u}{\partial t} - \kappa \frac{\partial^2 u}{\partial x^2} = A \quad (2)$$

The solution of equation (1) for a single-event faulting (Hanks et al., 1984; Hanks, 2000) is

$$u(x,t) = \alpha \ \mathrm{erf}\left(\frac{x}{2\sqrt{\kappa t}}\right) + bx \quad (3)$$

The solution of equation (1) for a multi-event faulting (Hanks et al., 1984; Hanks, 2000) is

$$u(x,t) = (\alpha + At)\,\mathrm{erf}\left(\frac{x}{2\sqrt{\kappa t}}\right) + \frac{Ax^2}{2\kappa}\left\{\mathrm{erf}\left(\frac{x}{2\sqrt{\kappa t}}\right) - \mathrm{sgn}(x)\right\} + \frac{Ax}{\kappa}\sqrt{\frac{\kappa t}{\pi}}e^{\frac{-x^2}{4\kappa t}} + bx \quad (4)$$

where

sgn (x) = +1	$x > 0$	A means uplift
sgn (x) = -1	$x < 0$	A means down drop

and for all x values α and A values will be positive (Hanks et al., 1984).

These models were applied using the Python code PyScarpFit (https://github.com/seanpolun/pyScarpFit). PyScarpFit locates the midpoint of the scarp (x=0) and identifies throw (2H) and far-field slope (α). When κ is known, the fault scarp can be dated; likewise, when the fault scarp age is known, the κ can be defined (Hanks et al., 1984).

The choice of which model to use (single-event vs steady state) can result in approximately a factor of two difference in total mass diffusivity (Hanks et al., 1984). In reality, these should be considered as end-member possibilities, unless a fault scarp can unambiguously be associated with a single, surface faulting event. Applying a single-event model to a multi-event (i.e., composite) fault scarp will underestimate the mass diffusion (and thus, if κ is known, the age is underestimated). On the other hand, the steady-state model, which assumes constant uplift balanced by constant erosion) may slightly overestimate the mass diffusion (and, consequently, the age) if the number of surface faulting events is small.

For the study area, fault scarp profiles along the Owl Lake Fault were modeled using the "steady-state" uplift model. The fault scarps corresponded with large lateral offsets that most likely represented multiple earthquake faulting events.

On the other hand, terrace riser profiles at the southwest end of the study area (i.e., the location studied by McGill [1993]) were modeled using single event solution to the differential equation. I believe this is appropriate, because the incision of a terrace riser is likely a short-lived event that starts after the abandonment of the upper terrace surface.

3.3. Low Altitude Photogrammetric Surveying

At one location at the northeast part of the fault, a low altitude photogrammetric survey was made (Figure 3-3) to assess the benefit of a dense point cloud (~1000 points per m^2) in comparison with the available LiDAR point cloud (4.6 points per m^2); producing a 0.5 meter-pixel DEM. A particular goal of low-altitude aerial surveying is assessing the smallest observable offsets (likely a single earthquake event) that might not be observable with the airborne LiDAR data.

Three-dimensional, photogrammetric mapping was accomplished using the Structure-from-Motion (SfM) algorithm as implemented in Agisoft Metashape software (www.agisoft.com). As discussed by Fonstad et al. (2013), SfM is similar to classical stereoscopic photogrammetry (e.g., Drury, 2004) in that three-dimensional-structures from two-dimensional-images. However, SfM is the simultaneous solves for the arrangement of the camera positions, as well as the scene geometry. Compared with classical stereoscopic photogrammetry (which uses pairs of overlapping photos), SfM requires 3 or more distinct camera positions with overlapping views. On the other hand,

SfM has an advantage in that camera positions can be arbitrarily oriented (as opposed to being parallel to the general surface, as required for classical stereo photogrammetry).

The low altitude aerial surveying involved a multi-rotor drone. Four ground control points (GCP) were placed within the survey area as reference points for the drone. With these GCPs, large areas can be accurately mapped by the drone. Locations of these GCPs (coordinates and elevations) were measured by rapid-static GNSS (Global Navigation Satellite Systems).

The drone used in this study was a DJI Phantom 4 Pro V2 using a 20-megapixel camera. The aircraft flew ~50 m above the ground level and acquired approximately 200 photographs during this survey. These captured photos were processed by using Agisoft Metashape. Drone positions in each photo capturing, four GCPs, and created point cloud is shown in Figure 4-18. The raw photogrammetric point cloud had a point spacing of approximately 2.3 cm, and this was resampled to create a 4-cm-pixel DEM (Figure 4-19) to map offsets. In addition to the DEM, an orthophoto mosaic (also 4-cm-pixel resolution) was also constructed from the photos.

3.4. Propagation of Measurement Uncertainty

Measured and modeled quantities are presented with corresponding uncertainties. Propagation of uncertainties in subsequent calculations is accomplished using arithmetic rules for normal (Gaussian) probability distributions (Geyh & Schleicher, 1990). The arithmetic rule for calculating averages and standard deviation is:

$$\sigma = \left(\frac{1}{\sigma 1^2} + \frac{1}{\sigma 2^2} + \cdots + \frac{1}{\sigma n^2}\right)^{-1/2} \quad (5)$$

$$\mu = (\sigma^2((\frac{\mu 1}{\sigma 1})^2 + (\frac{\mu 2}{\sigma 2})^2 + \cdots + (\frac{\mu n}{\sigma n})^2))^{1/2} \quad (6)$$

where μ is mean value and σ is standard deviation, and subscripts denote individual measurements.

The arithmetic rule for division of normal probabilities is:

$$\frac{\mu 1 \pm \sigma 1}{\mu 2 \pm \sigma 2} = \frac{\mu 1}{\mu 2} \pm \frac{\mu 1}{\mu 2}\sqrt{(\frac{\sigma 1}{\mu 1})^2 + (\frac{\sigma 2}{\mu 2})^2} \quad (7)$$

On a final note, although some of these values likely represent uniform probability distributions (e.g., measured fault offset), these were treated as normal probability distributions for the benefit of computation.

Table 3-1. Variables

Variable	Variable Meanings	Units
2H	Scarp height	m
κt	Total degradation	m^2
κ	Mass diffusivity	m^2/kyr
t	Time (Age)	kyr
μ	Mean value	-
σ	Standard deviation	-

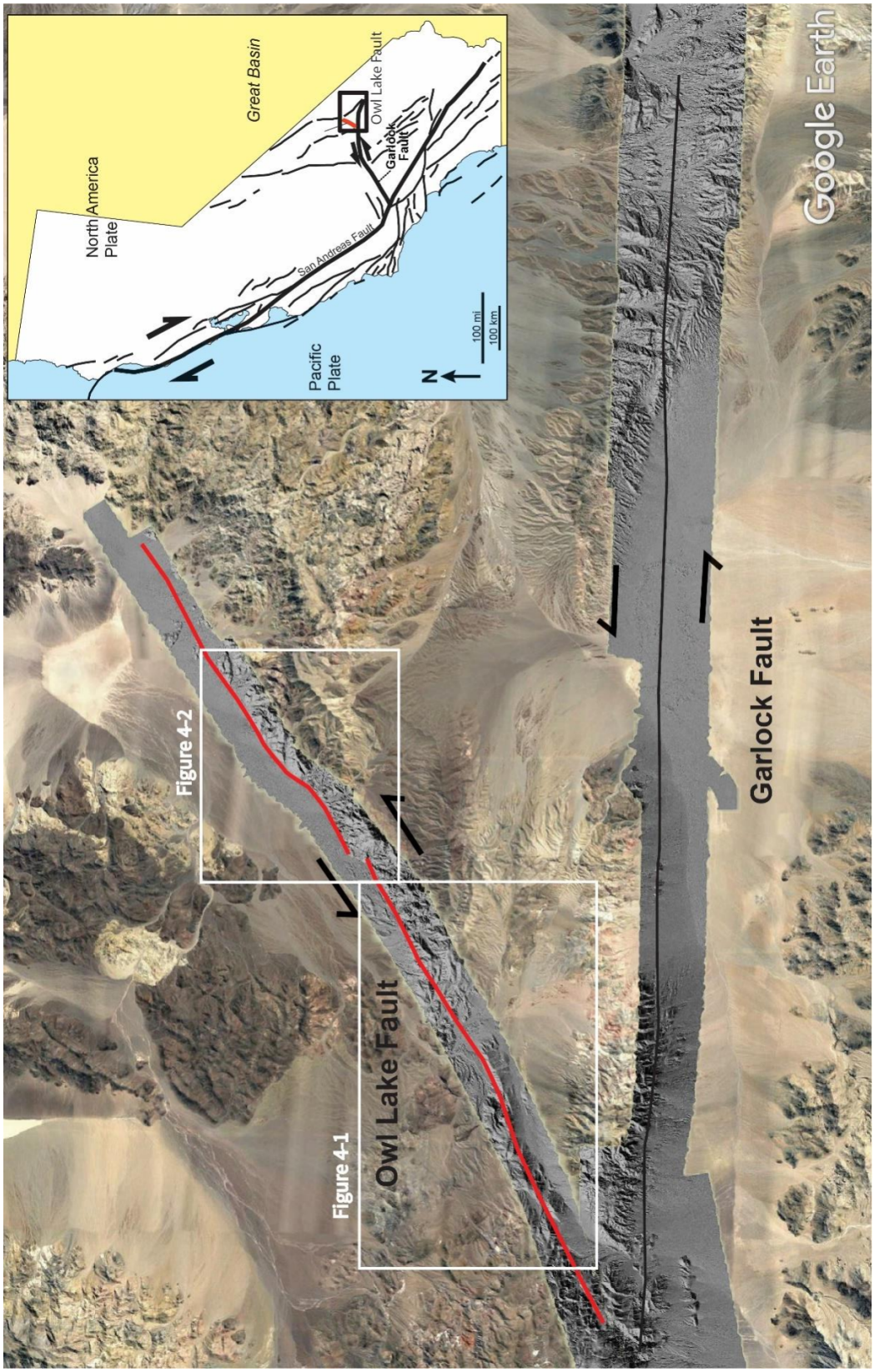

Figure 3-1. The Overview of the Owl Lake Fault and the Garlock Fault with LiDAR

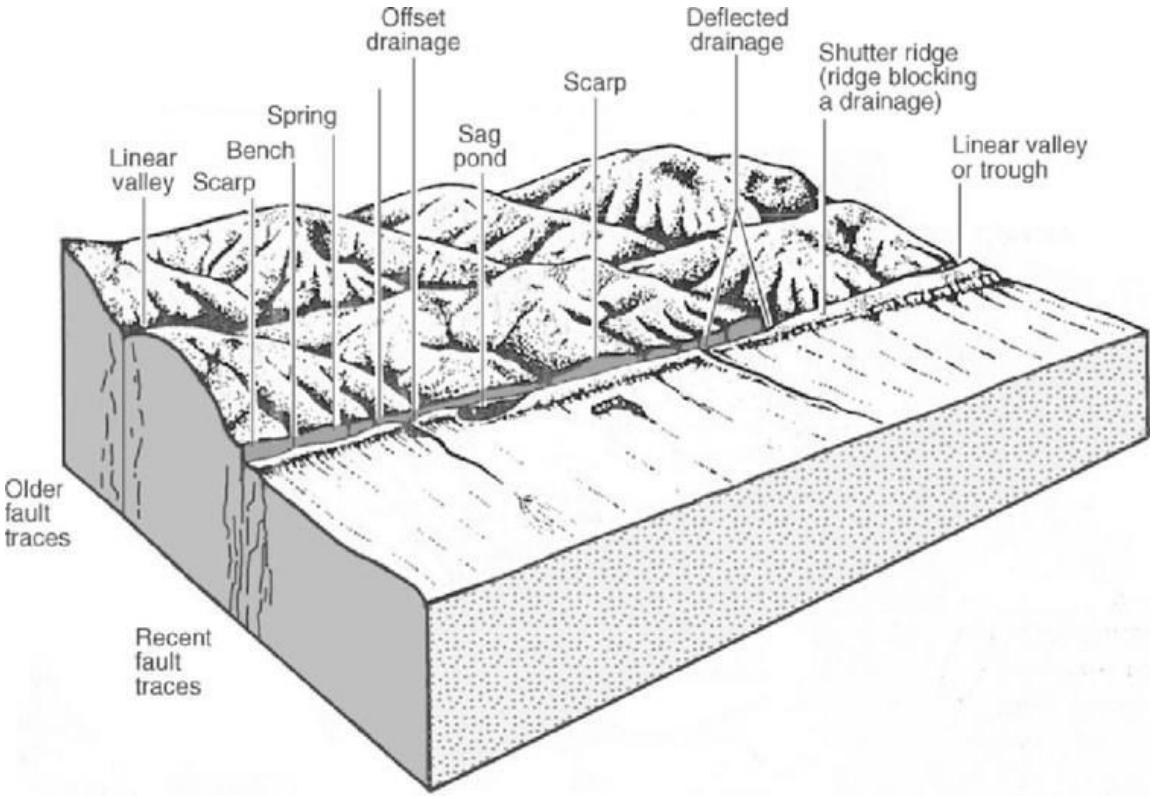

Figure 3-2. Landforms Developed along Strike-Slip Faults. Adapted from Wesson et al., 1975.

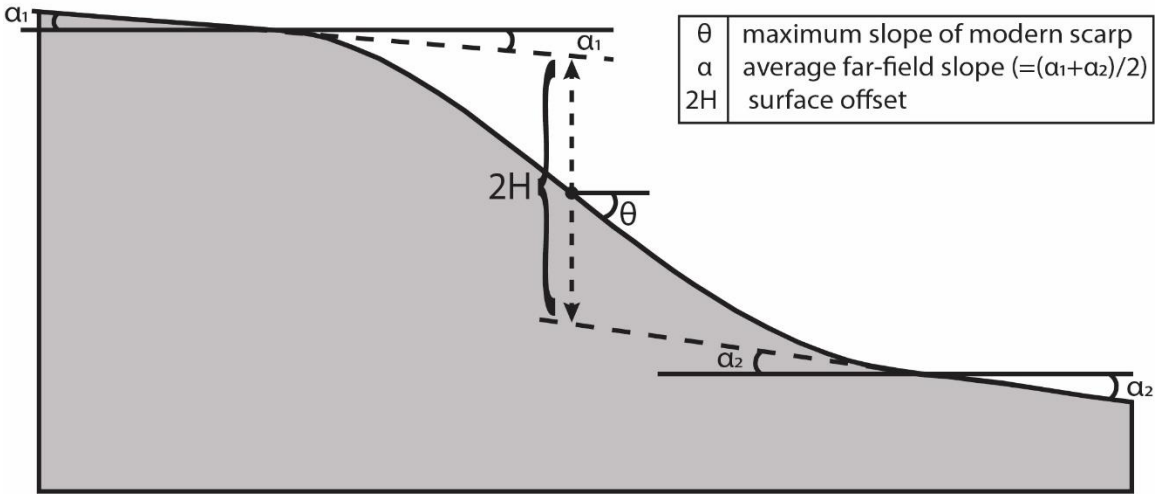

Figure 3-3. Illustration of the cross section across a fault scarp

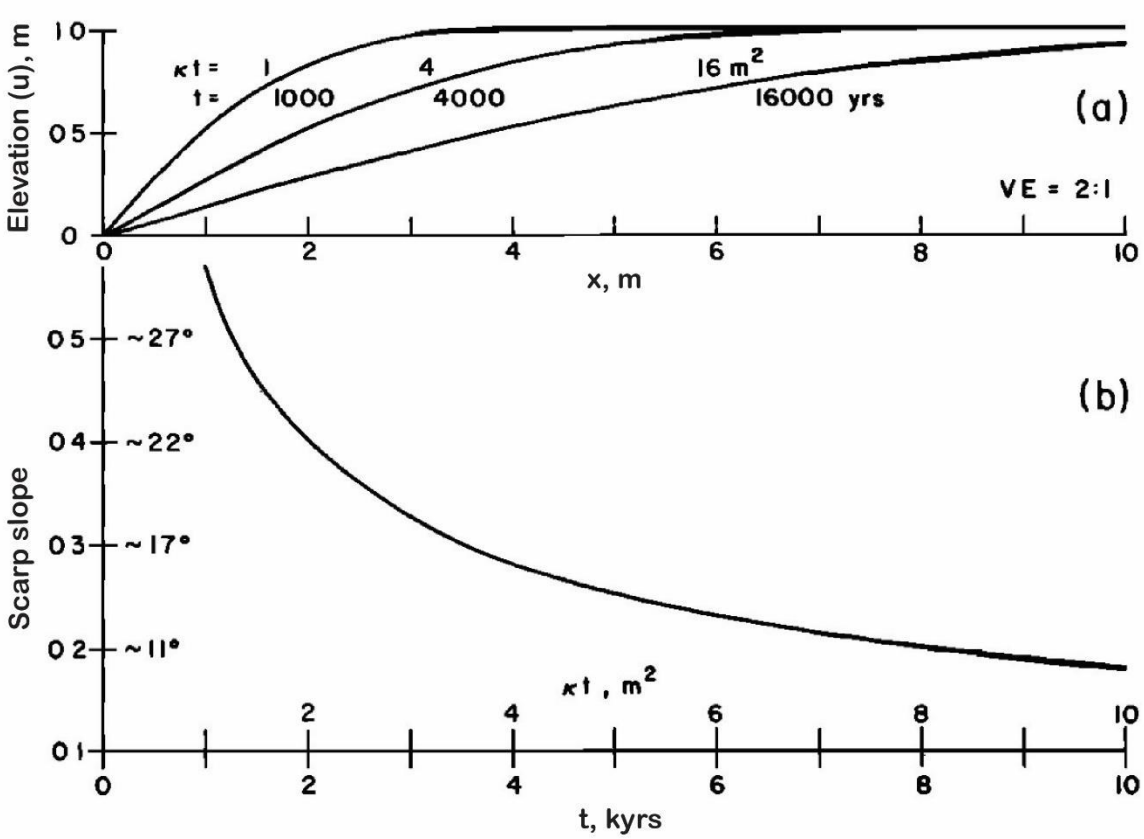

Figure 3-4. Evolution of a scarp, modified from Hanks et al., 1984.

4. RESULTS

4.1. Fault Offsets

The mapped fault is shown in Figure 4-1 and 4-2. In addition to delineating the fault traces, large fault-related landforms (e.g., likely offset stream valleys) were identified, as well as other landscape features affected by faulting.

To calculate lateral slip rate of the Owl Lake Fault, left-laterally offset stream channels and landforms (such as alluvial fan) were observed and measured from the available image data. These lateral displacements were measured from geomorphic surfaces whose ages were estimated from the modeled fault scarp profiles for each location (see below). All locations are shown on the fault map in Figure 4-1 and 4-2.

Location #1 shows two stream channels with large, leftward deflections of similar magnitude (Figure 4-3), which are interpreted as offsets that have accumulated after the deposition of the alluvial fan in which they incise. After accounting for possible, subsequent erosion of the channel wall as the downstream side shifts by faulting, the lateral displacements were measured as 42-60 m and 65-74 m, respectively.

The Quaternary features from the surface at Location #2 may not provide reliably measurable horizontal offsets (Figure 4-4), although the fault lineament and fault scarps are very clear. It is possible that the edge of the alluvium may be offset range from 6 to 12 m., but this may be inaccurate owing to subsequent lateral erosion of stream channels. Therefore, the slip rate from this location is not reliable and will likely underestimate the slip rate of the Owl Lake Fault.

At the location #3, a small alluvial fan was identified juxtaposed by the fault against the channel that likely fed it sediment (Figure 4-5, 4-6). Lacking any apparent offset stream channels or terrace features, left-lateral offset was assessed by examining possible displacement of the alluvial fan apex (i.e., location of initial deposition) from the source channel, following the method presented by Keller & Pinter (2002). To accomplish this, the LiDAR DEM was contoured with 1-m intervals by the ArcGIS Pro, and ellipses were fit to contours on the fan surface (Figure 4-6). The elliptical fits (rather than circular fits) suggest possible tilting, and the major axes generally align to indicate the fan apex (Figure 4-6, green arrow). This apex line serves as a piercing point (i.e., a reference point to measure the offset) for comparison with the upstream channel that fed the sediment. Owing to the large channel width, this site was expected to provide only a minimum estimate of fault offset (Figure 4-6, yellow arrows) and 40 m offset (Figure 4-6, blue arrow) seems unreliable.

At Location #4, the Owl Lake Fault trace has a large step between two distinct branches (Figure 4-7). This corresponds with a very large stream deflection (around 200 meters) that may be a long-term fault offset, but this feature cannot be confidently dated. However, smaller offsets in younger alluvial deposits are apparent along the scarp of the southeastern fault branch. The contact between the two alluvial deposits is apparent with a change in color in the NAIP imagery, as well as a difference in height of the fault scarp across the two deposits. The left-lateral offset of the contacts is measured to 6 to 15 m (Figure 4-8). However, this may not represent the complete recent slip of this part of the Owl Lake Fault, owing to the presence of the other (northwestern) fault branch.

Location #5 is the same location studied by McGill (1993) – this location is within the Fort Irwin military reservation, which makes it difficult to access in person. At this site, McGill identified several older alluvial units separated terrace risers. Adapting McGill's initial mapping with the detailed topography from the LiDAR and NAIP imagery, these two terrace risers (i.e., the vertical face separating adjacent stream terrace surfaces) were remapped (Figure 4-9). Left-lateral offsets were measured to be 18-19 m and 70-80 m, respectively. Although McGill (1993) had suggested a maximum offset of 235 m, this does not seem likely, as this would shift the terrace riser to a location without a sufficient drainage upstream to be the source of the deposited sediment.

4.2. Fault Scarp Ages and Slip Rate

4.2.1. κ Calibration

For the study area κ (the mass diffusivity constant) is unknown, but it can be calibrated based on studies conducted in an area with similar geological and climatic conditions. For this part of the research, results were used from the dating studies on displaced alluvial fans by normal faults at Badwater by Frankel et al. (2015). Owl Lake and Badwater have similar climatic conditions (Koppen Climate Classification, BWh). Badwater receives approximately 50 mm/yr of precipitation (https://www.nps.gov/deva/planyourvisit/weather.htm), which is less than the Owl Lake study area (80-90 mm/yr, see Chapter 2). This may result in slight underestimation of κ for the Owl Lake area. With that caveat, owing to the proximity, Badwater may be the most appropriate site with reliable age control for calibration of the mass diffusivity constant.

To determine the κ value, three degradation profiles were located on a dated alluvial fan at the Qg3a surface. The surface is described as "moderately cemented conglomerate with moderate varnished clasts" by Frankel et al., 2015. The first profile from the Qg3a surface (Qg3a1) cuts two scarps, so this profile was modeled for each fault scarp as Qg3a1a and Qg3a1b, and the last profile was modeled as Qg3a2 for both single and multi-events (Figure 4-10, 4-11, 4-12). These three profiles were processed for both single- and multi-event degradation models to obtain diffusion parameters H and κt (Table 3-2).

Using the average of the κt values (μ: mean value) and uncertainties (σ: standard deviation) from the Qg3a surface at Badwater Basin (Table 3-2) with the averaging equations (5) and (6), average κt is calculated as 1.1 ± 0.2 m^2.

To calculate the κ for this region, the κt value should be divided to surface age using division equation (7). Frankel et al. (2015) date the Qg3a alluvial fan using Optically Stimulated Luminescence (OSL) method as 4.5 ± 1.2 ka. Using equation (7), κ is calculated as 0.3 ± 0.1m^2/kyr. I assume that this value will be applicable to Owl Lake, owing to proximity and similar climate conditions.

4.2.2. Ages and Slip Rates

Four profiles were extracted from the LiDAR point cloud at three locations to estimate ages of faulted surface along the Owl Lake Fault. In locations where the observed faults appear to capture all of the slip along the Owl Lake Fault, these ages permit calculation of possible rates of fault slip. At each area, profiles were selected for modeling that (1) did not show evidence of local gullying or other stream incision, and

(2) appear to satisfy the requirement of along-profile sediment transport. These profiles were named starting from NE (profile #12) to SW (profile #54), indicating the location number and the profile number, respectively. Profile #52 and #54 were extracted from the terrace riser where McGill (1998) determined the slip rate of the Owl Lake Fault.

For each profile, LiDAR points were extracted for a swath a width of 0.5 to 1.0 m from the bare-earth point cloud. As a result of the modeling process, diffusion parameters κt (total degradation) and 2H (scarp height – throw) values for single and multi-events were obtained from the seven degraded fault scarp profiles (Table 3-1, Figure 4-13, 4-14, 4-15, 4-16, 4-17).

Extracted profiles along the Owl Lake Fault provide the vertical displacement values (2H) with uncertainties (σ) as represented in Table 4-2. Slip rates for vertical displacements were calculated applying the equation (7) with 2H values and ages for each profile. Obtained dip-slip rate results were listed in Table 4-5. According to these results, the dip-slip rate ranges from 0.04 ± 0.03 mm/yr to 0.15 ± 0.09 mm/yr along the Owl Lake Fault.

The ages for each location were used to calculate the lateral slip rate of the Owl Lake Fault by using the division of normal probabilities (Equation 7). Calculated slip rates for each location with the uncertainties are listed in table 4-6. Gray lines in the table represent the slip rates that will not be used to estimation for the Owl Lake Fault. According to the results of these calculations, slip rates range from 0.8 ± 0.3 mm/yr to 2.3 ± 1.1 mm/yr.

4.3. Photogrammetrically Determined Offsets

Several offsets were measured from the photogrammetric survey by using combination of shaded topography (Figure 4-19), detailed contour lines (25-cm contour interval), and the orthophoto mosaic (Figure 4-20). For the shaded relief images, low sun angle was applied to produce shadows and highlights the fault traces and possible offsets. Measured offsets are shown in Figure 4-19 with the main fault and its splays.

The most noticeable are the largest offsets, which ranges from 2.3-2.8 m to 27.4-31.7 m. These are consistent with features observed from the lower resolution LiDAR data, previously presented with the 0.5-m-pixel DEM. Importantly, the higher resolution, drone-derived data allow confident identification of minimum gully offsets that have range from 0.9-1.4 m to 1.6-2.0 m. I interpret these to represent the displacement of a single slip event (i.e., the last surface-rupturing earthquake). The average single-event displacement on the fault is calculated to be 1.6 ± 0.1 m, using Equations 5 & 6.

Table 4-1. Extracted profiles from Badwater area, Frankel et al., 2015

Single Event					
Profile no	**2H (m)**		σ	**κt (m^2)**	σ
Qg3a1a	1.84	±	0.06	1.3 ±	0.5
Qg3a1b	1.90	±	0.06	1.1 ±	0.3
Qg3a2	2.32	±	0.06	1.1 ±	0.4
Steady State					
Profile no	**2H (m)**		σ	**κt (m^2)**	σ
Qg3a1a	1.84	±	0.07	3.5 ±	1.6
Qg3a1b	1.92	±	0.06	2.5 ±	0.8
Qg3a2	2.32	±	0.05	2.7 ±	0.8

Table 4-2. Fault scarp degradation model results along the Owl Lake Fault

Steady State					
Profile no	**2H (m)**		**σ**	**κt (m^2)**	**σ**
Profile 12	3.18	±	0.08	22.1 ±	5.5
Profile 22	2.44	±	0.02	4.9 ±	0.6
Profile 32	0.46	±	0.01	1.2 ±	0.4
Profile 41	2.38	±	0.05	14.2 ±	3.1
Profile 42	1.28	±	0.02	6.7 ±	1.2
Single Event					
Profile 52	4.70	±	0.06	15.9 ±	1.6
Profile 54	1.76	±	0.02	7.0 ±	0.9

Table 4-3. Calculated ages from each profile along the Owl Lake Fault using calibrated κ=0.3±0.1 m2/kyr

Steady State					
Profile no	**κt (m^2)**		**σ**	**Age (kyr)**	**σ**
Profile 12	22.1	±	5.5	73.7 ±	30.6
Profile 22	4.9	±	0.6	16.3 ±	5.8
Profile 32	1.2	±	0.4	4.0 ±	1.9
Profile 41	14.2	±	3.1	47.3 ±	18.9
Profile 42	6.7	±	1.2	22.3 ±	8.5
Single Event					
Profile 52	15.9	±	1.6	53.0 ±	18.5
Profile 54	7.0	±	0.9	23.3 ±	8.3

Table 4-4. Calculated dip-slip rates along the OLF

Profile no	2H (m)	σ	Age (kyr)	σ	Dip Slip (mm/yr)	
Profile 12	3.18	± 0.08	73.7	± 30.6	0.04	± 0.03
Profile 22	2.44	± 0.02	16.3	± 5.8	0.15	± 0.09
Profile 32	0.46	± 0.01	4.0	± 1.9	0.12	± 0.08
Profile 41	2.38	± 0.05	47.3	± 18.9	0.05	± 0.03
Profile 42	1.28	± 0.02	22.3	± 8.5	0.06	± 0.04
Profile 52	15.9	± 1.6	53.0	± 18.5	0.09	± 0.05
Profile 54	7.0	± 0.9	23.3	± 8.3	0.08	± 0.05

Table 4-5. Calculated left lateral slip rates along the Owl Lake Fault

Profile no	Offset (m)	Age (kyr) σ	Slip Rate (mm/yr) Left Lateral
Location #1	58 ± 5	73.7 ± 30.6	0.8 ± 0.3
Location #3	9	4.0 ± 1.9	2.3 ± 1.1
Location #5-1	70 ± 5	53.0 ± 18.5	1.3 ± 0.5
Location #5-2	18.5 ± 0.5	23.3 ± 8.3	0.8 ± 0.3

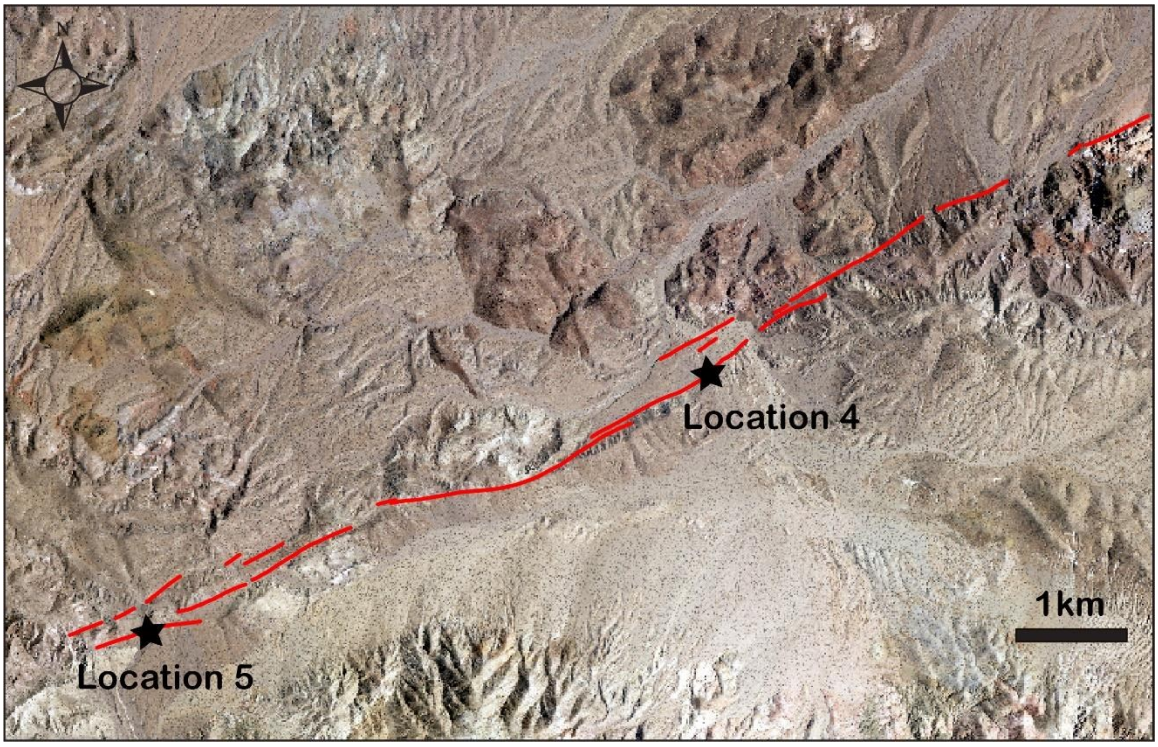

Figure 4-1. Mapping of the OLF -1: southwest end of the fault and profile locations

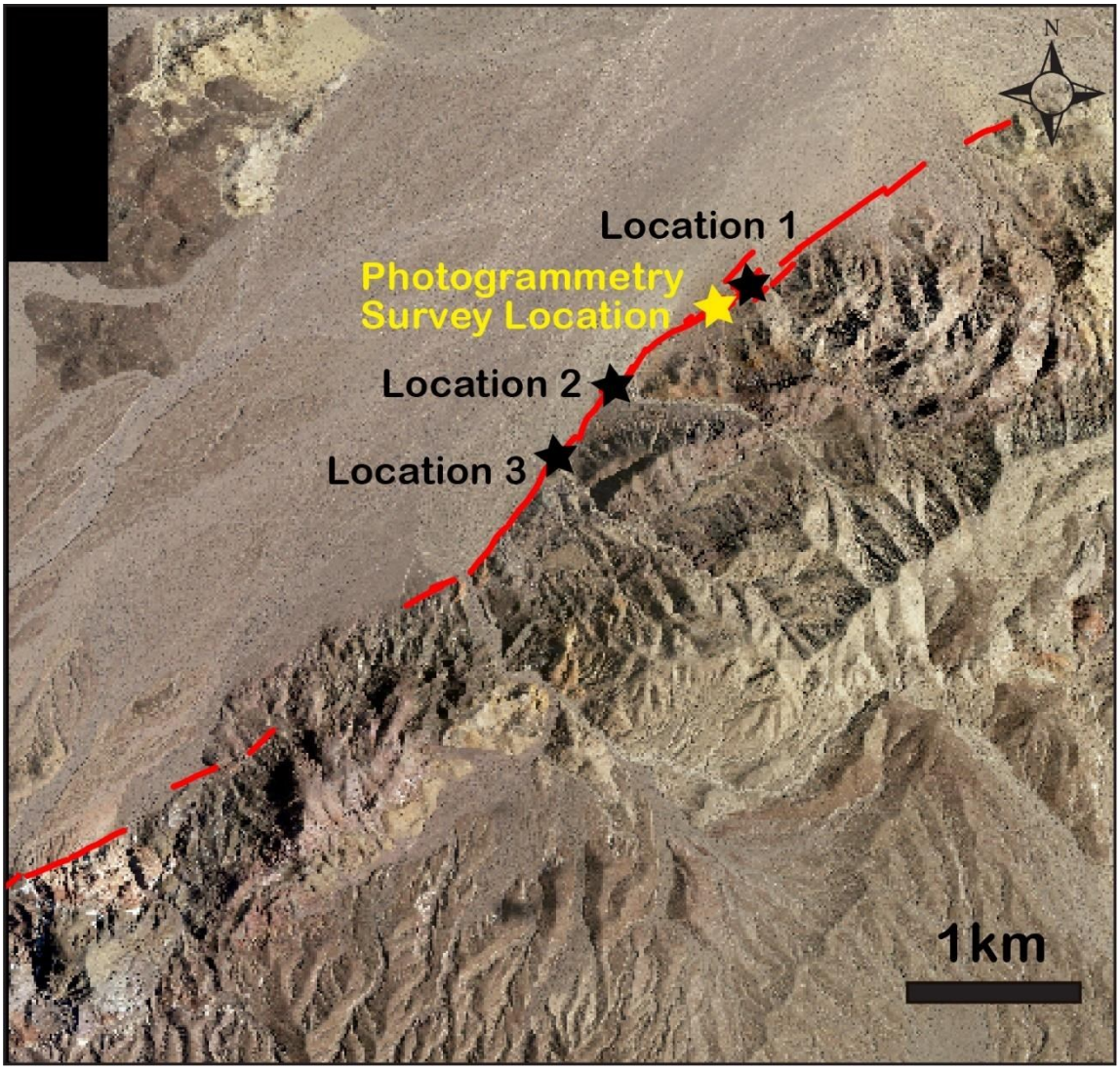

Figure 4-2. Mapping of the OLF -2 : northeast end of the fault and profile locations

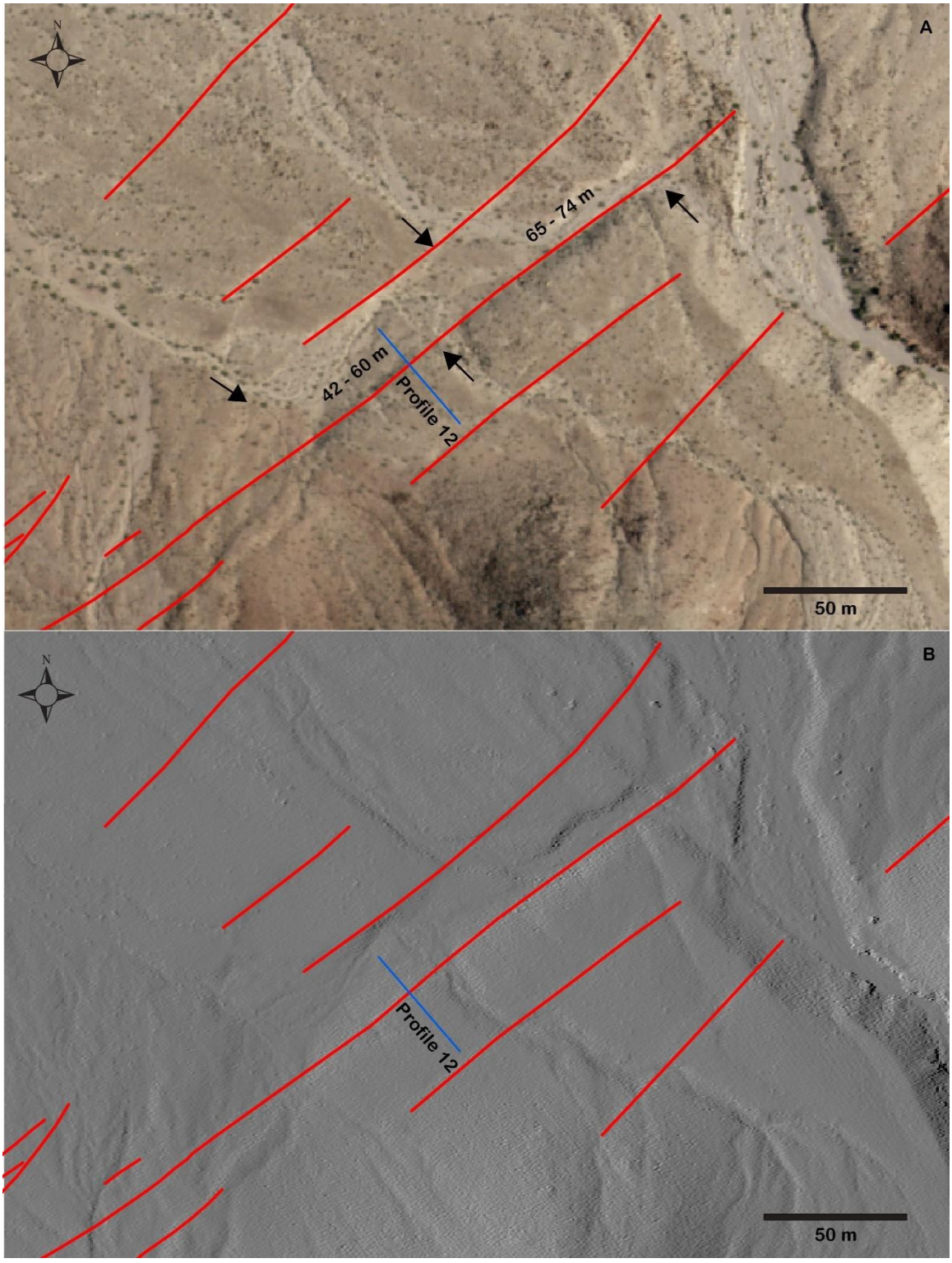

Figure 4-3. Location #1, profile 12, and possible offsets. Red lines: The main fault and its splays, black arrows: Offsets. A: NAIP image, B: Shaded relief image from LiDAR

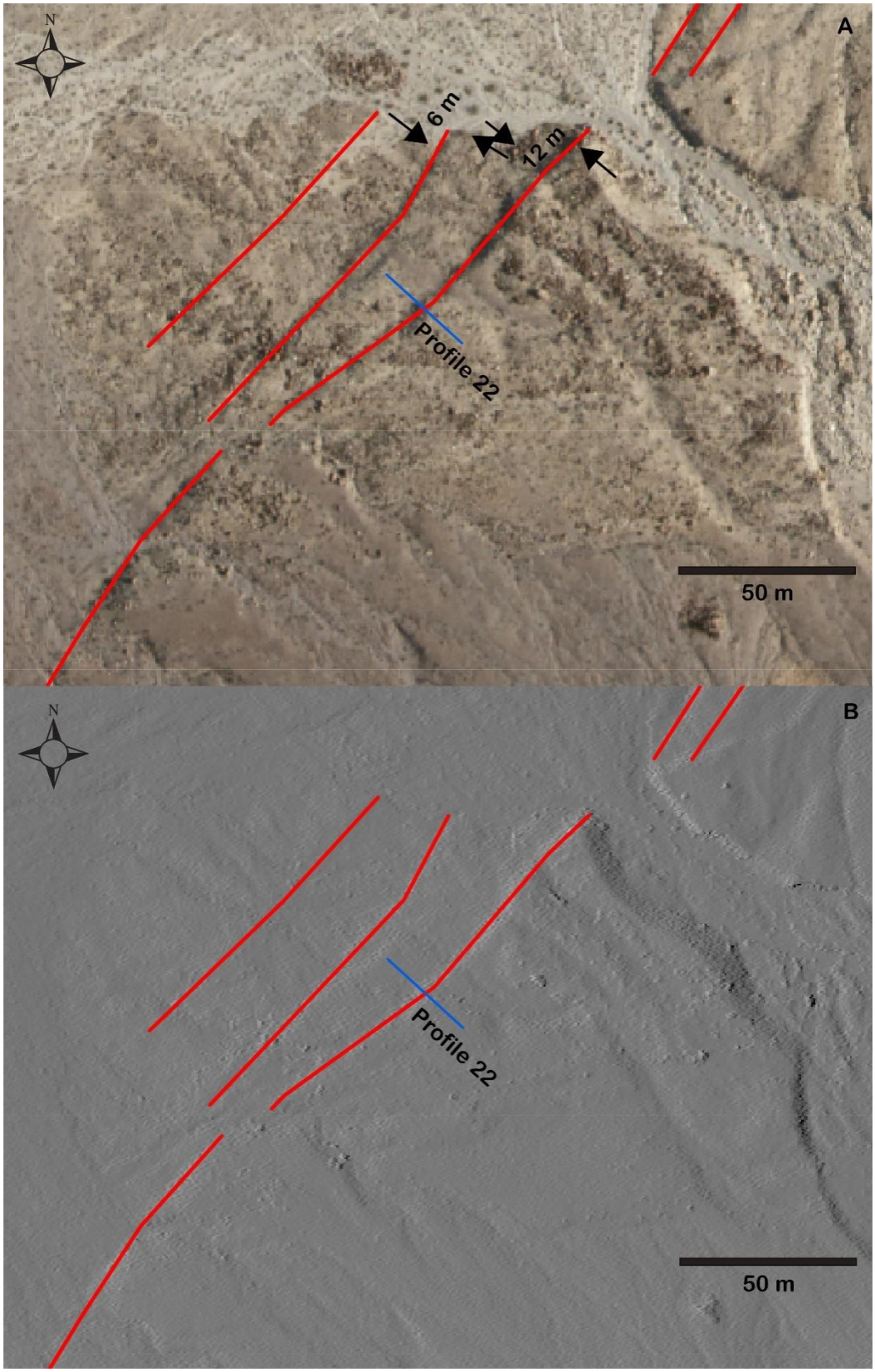

Figure 4-4. Location #2, profile 22, and possible offsets. Red lines: The main fault and its splays, black arrows: Offsets. A: NAIP image, B: Shaded relief image from LiDAR

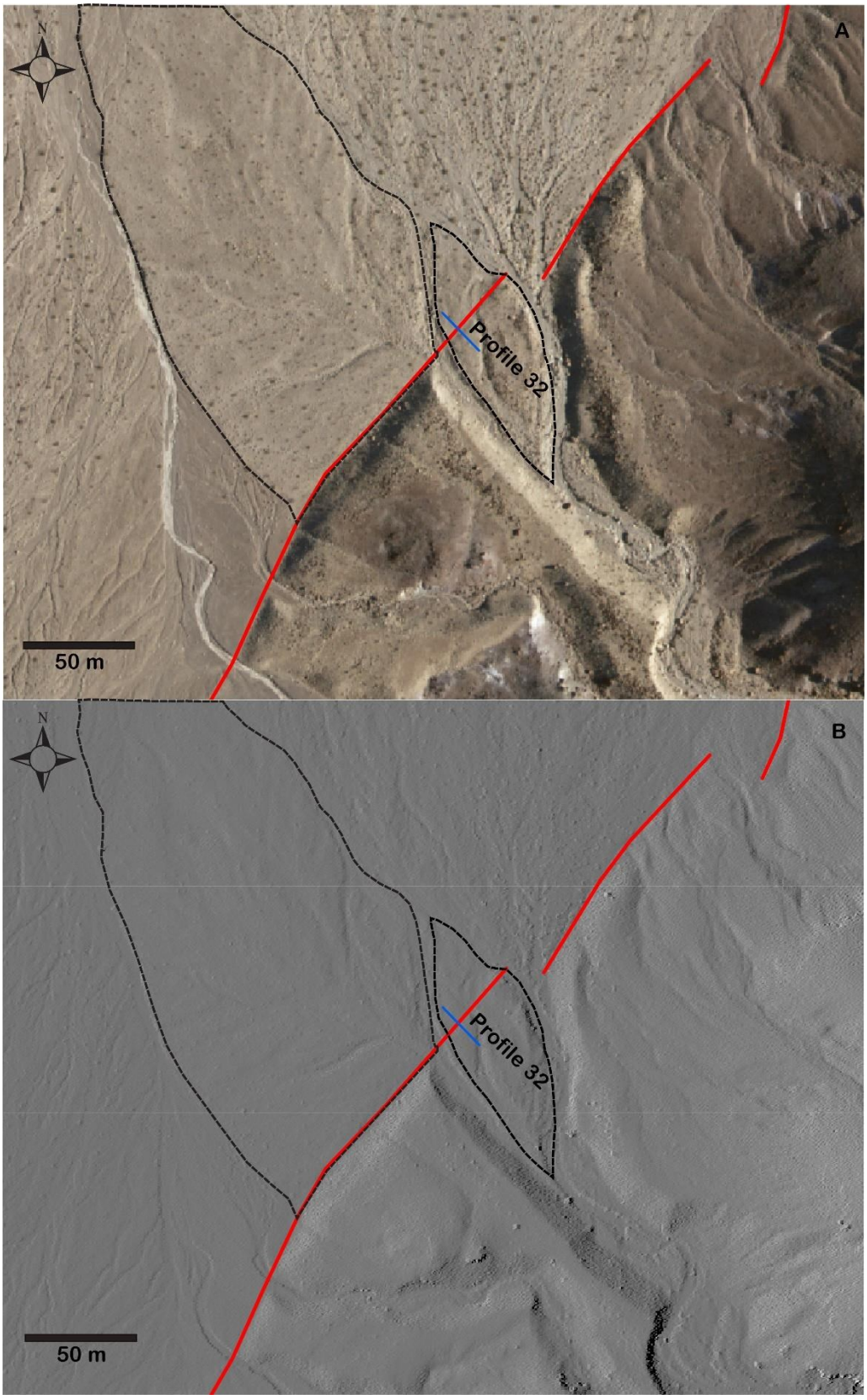

Figure 4-5. Location #3 profile 32, and alluvial fan. Red lines: The main fault and its splays, black arrows: Offsets. A: NAIP image, B: Shaded relief image from LiDAR

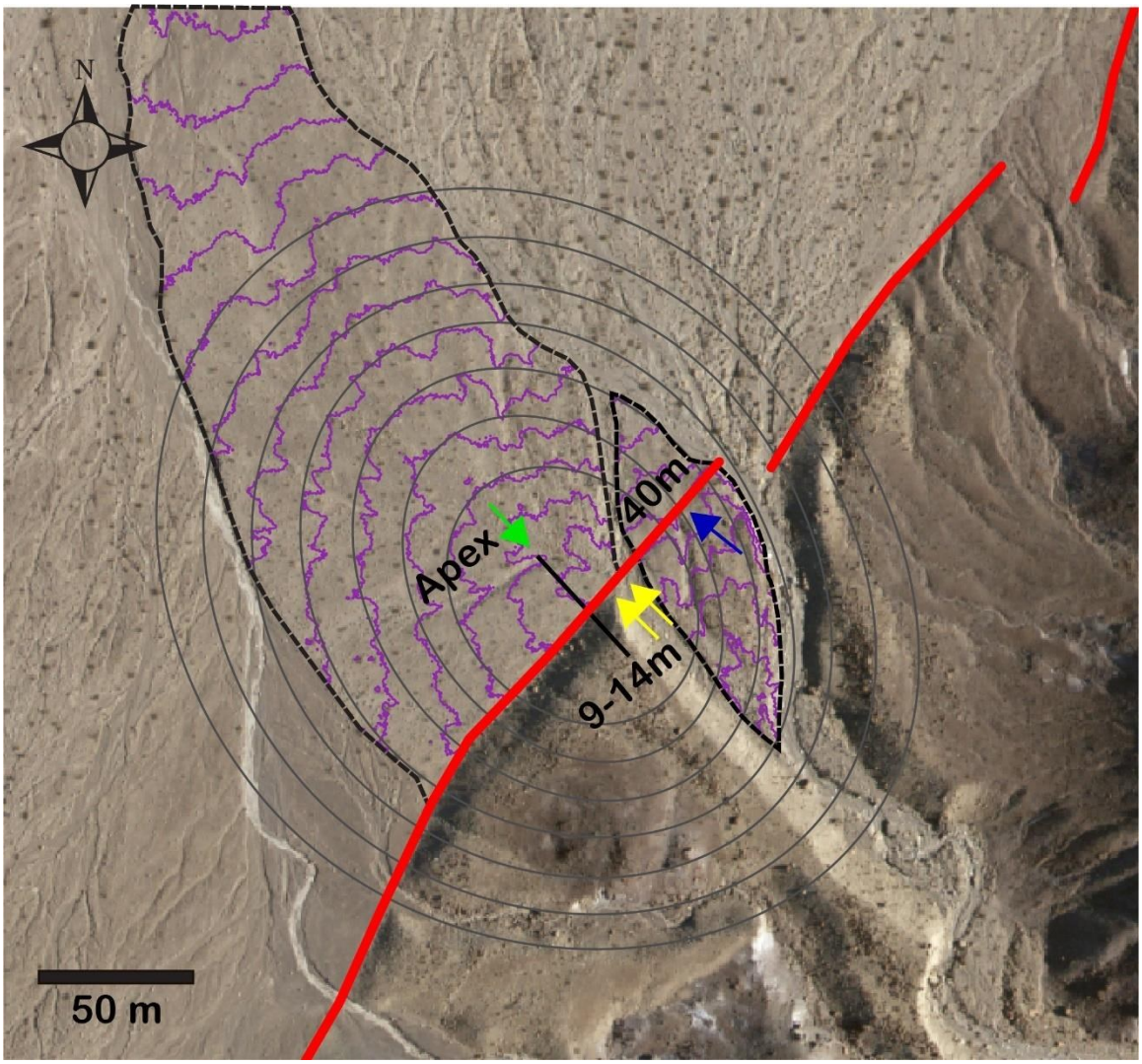

Figure 4-6. Location #3, alluvial fan. contour lines, elliptical arcs that fit the contour lines, and offsets. Green arrow shows apex, yellow arrows show possible offsets (9-14m, min. offset 9m), blue arrow shows unreliable offset (40m).

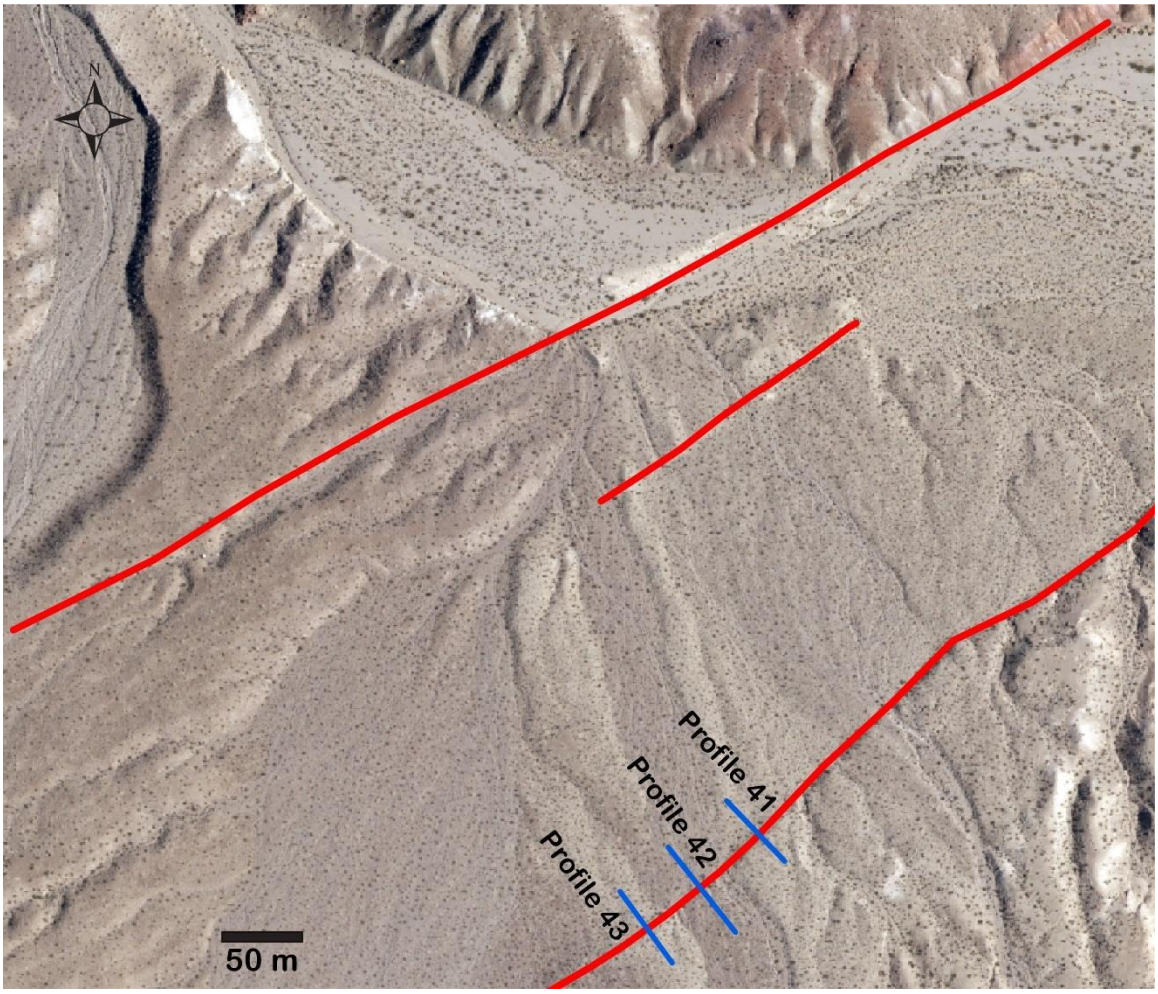

Figure 4-7. Location #4 the stepover of the Owl Lake Fault

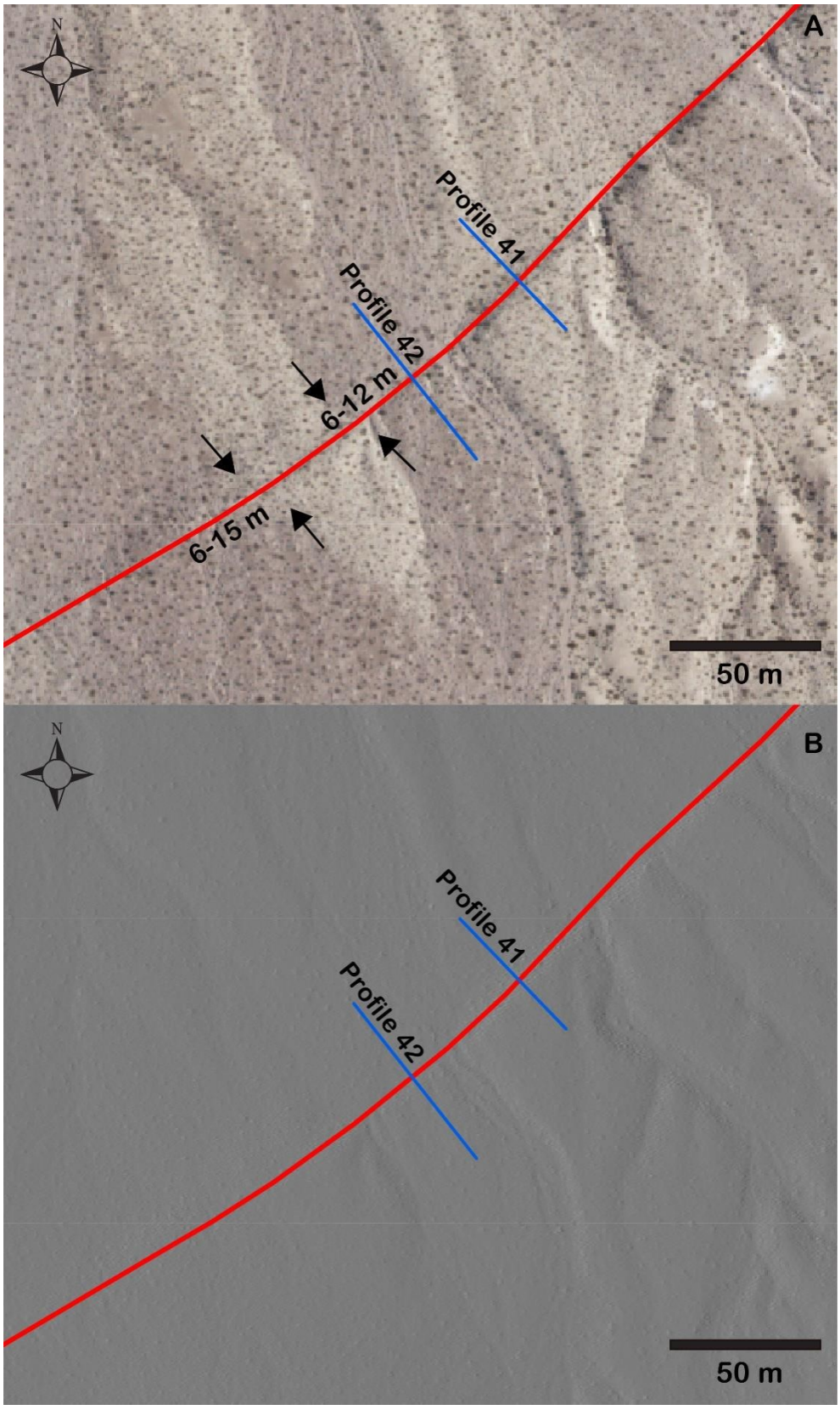

Figure 4-8. Location #4, profiles 41 and 42, and possible offsets. Red lines: The main fault and its splays, black arrows: Offsets. A: NAIP image, B: Shaded relief image from LiDAR

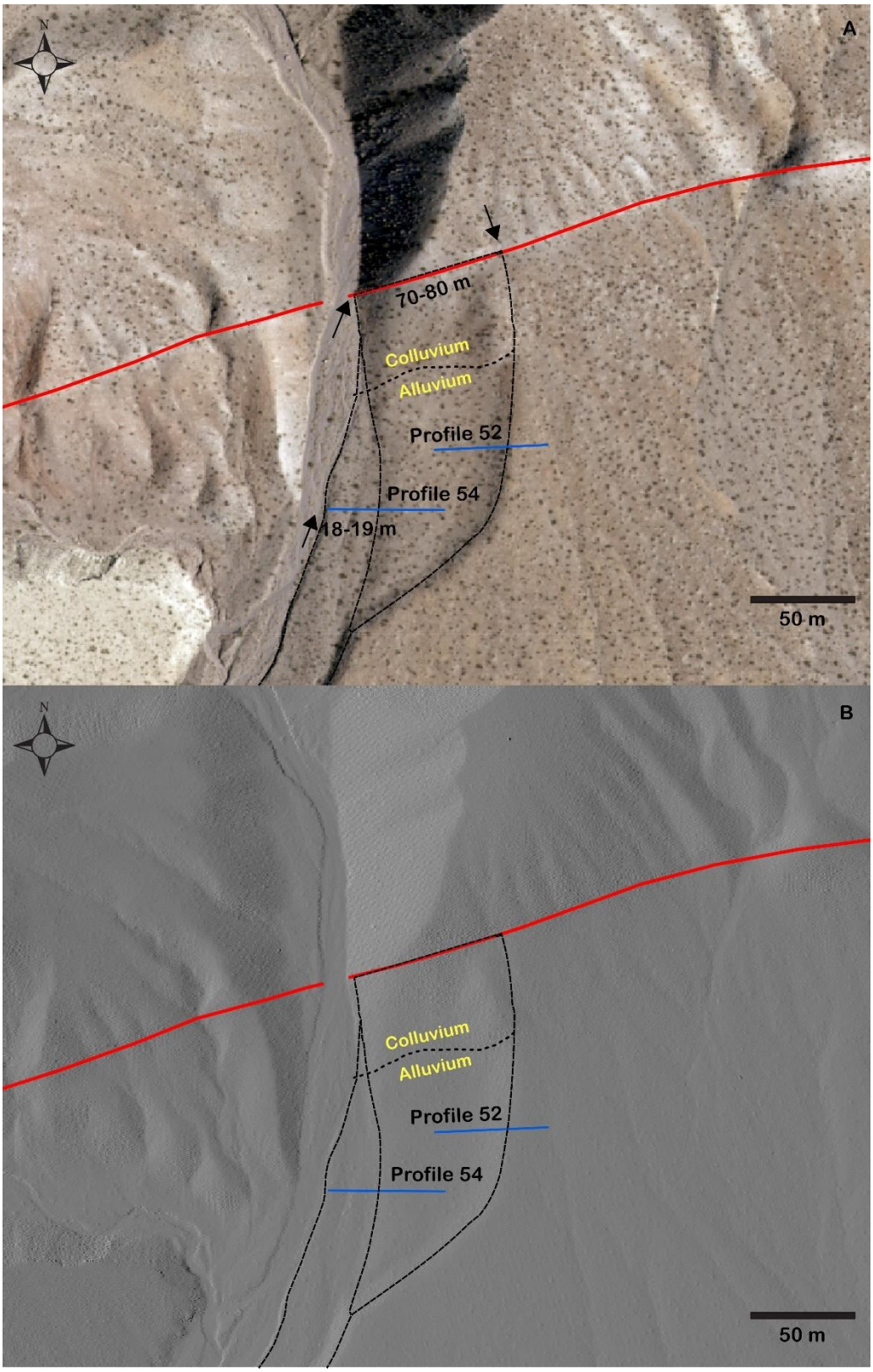

Figure 4-9. Location #5, McGill's study area (1998), profiles 52 and 54, terrace risers and possible offsets. Red lines: The main fault and its splays, black arrows: Offsets. A: NAIP image, B: Shaded relief image from LiDAR

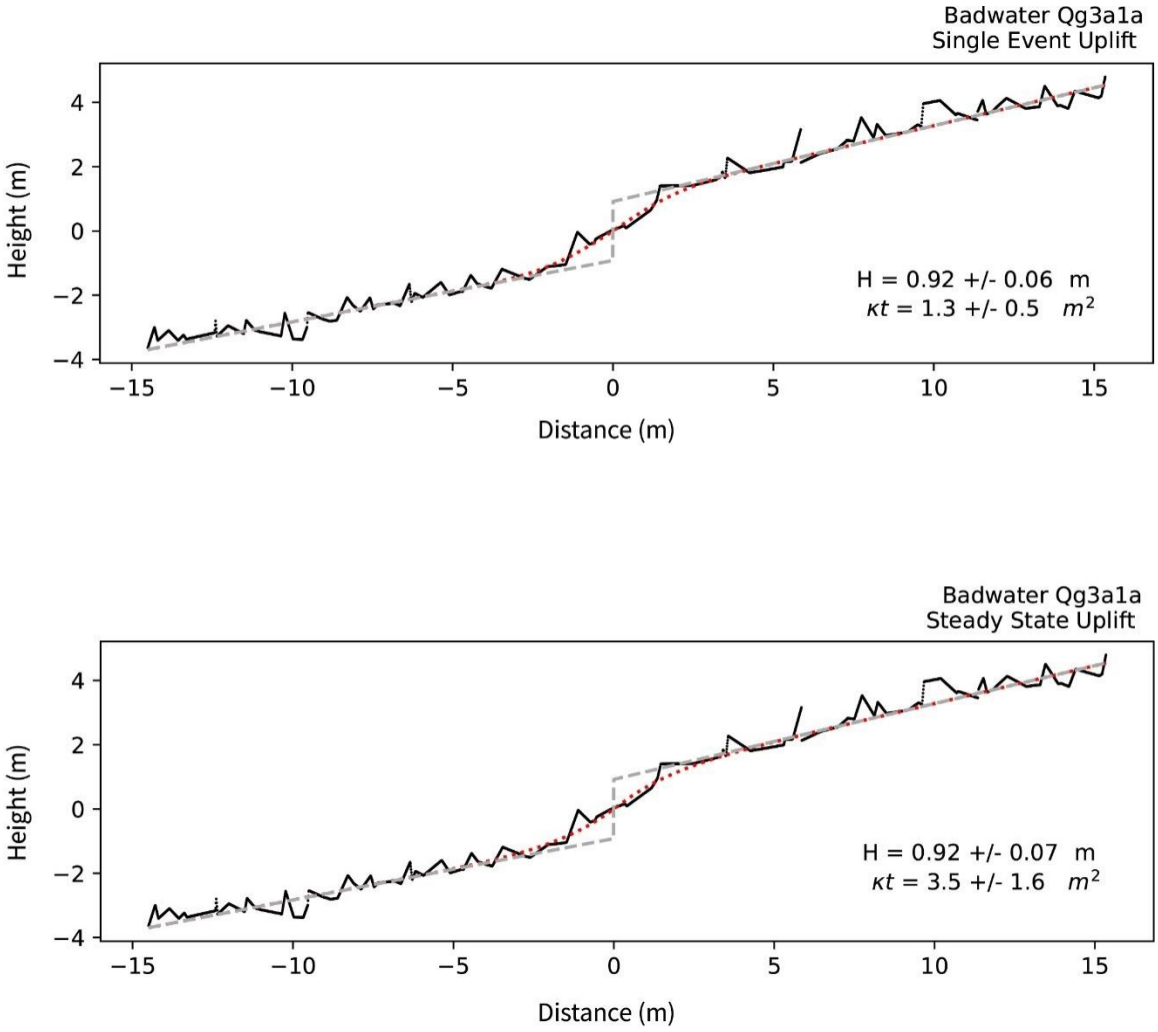

Figure 4-10. Extracted profile Qg3a1a for single-event and steady state

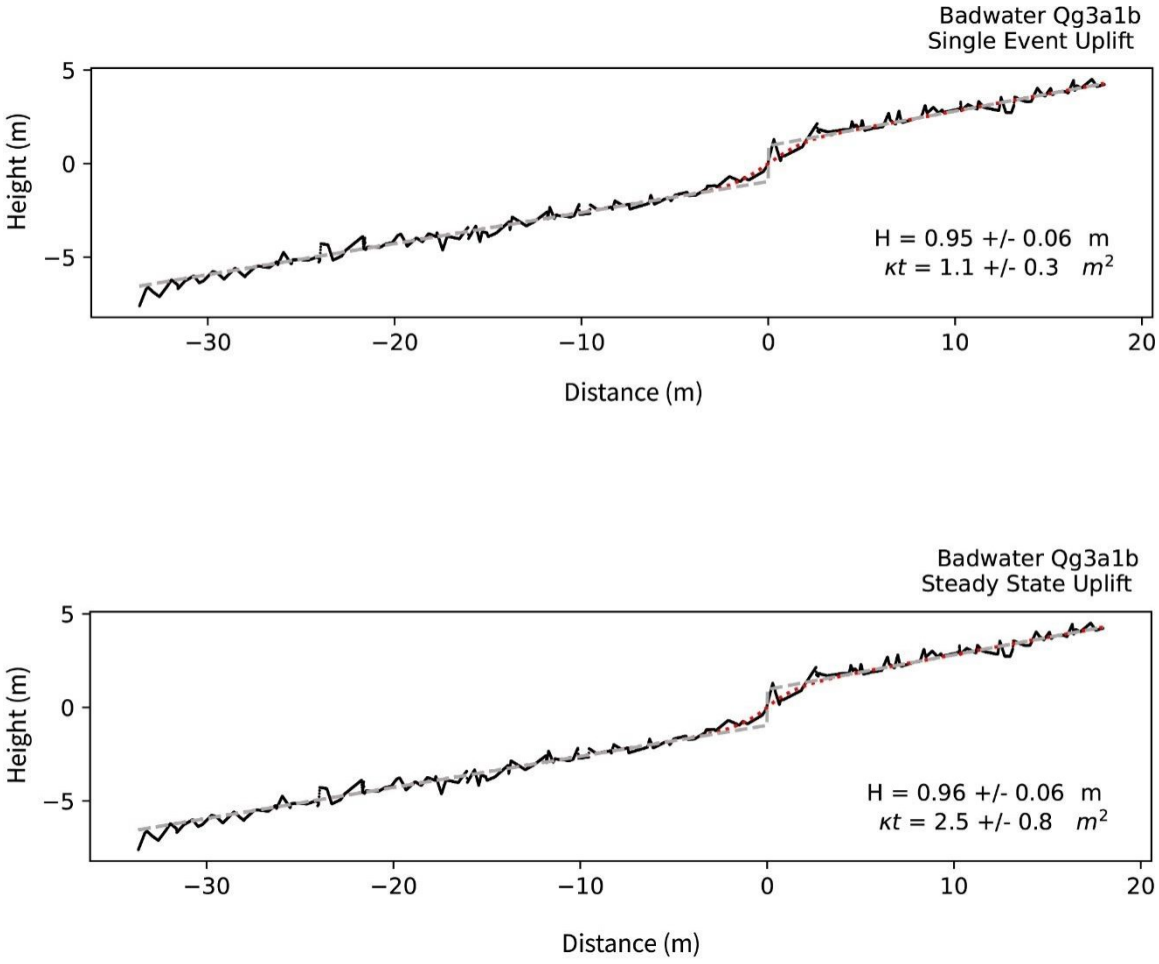

Figure 4-11. Extracted profile Qg3a1b for single-event and steady state

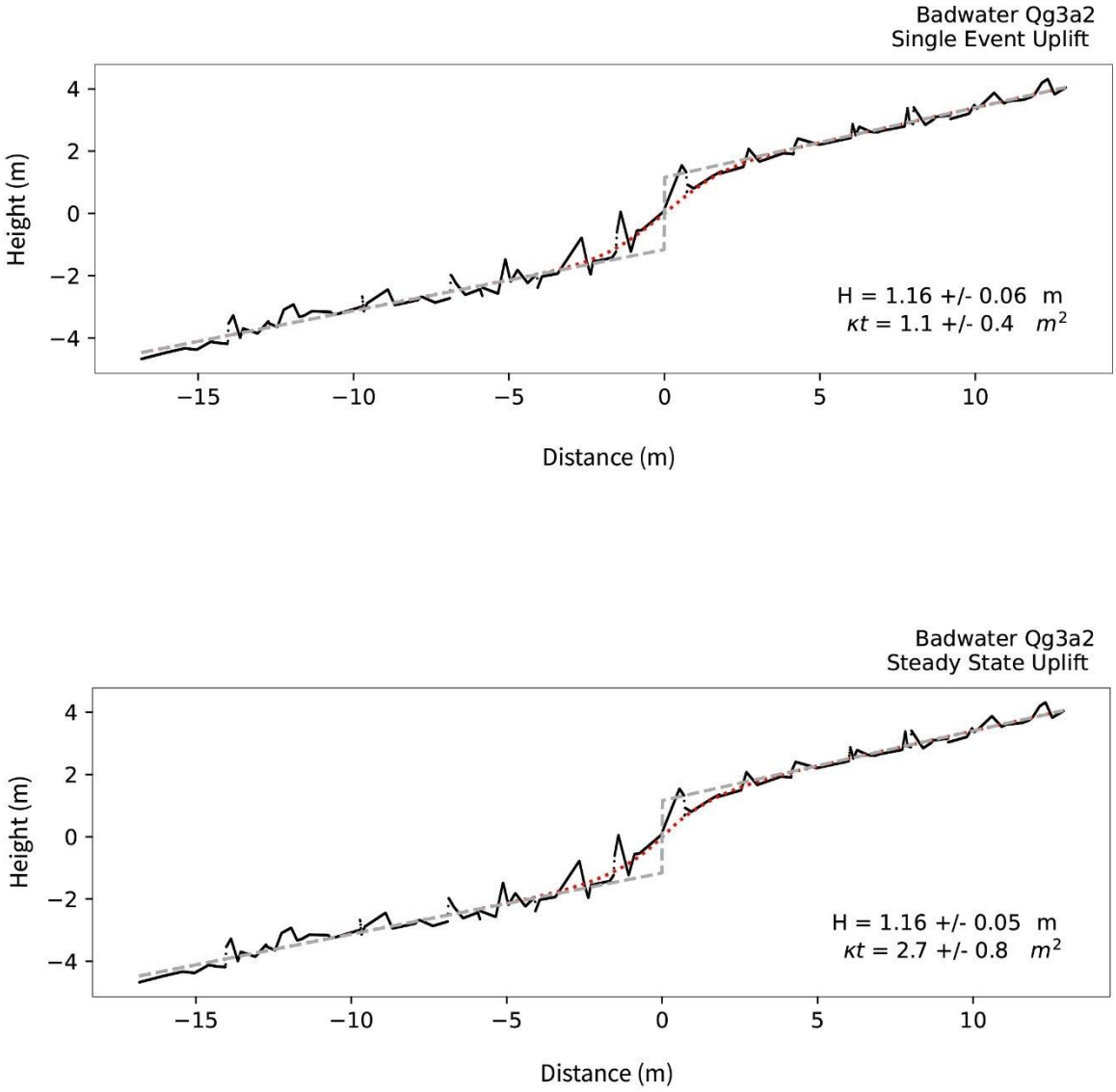

Figure 4-12. Extracted profile Qg3a2 for single-event and steady state

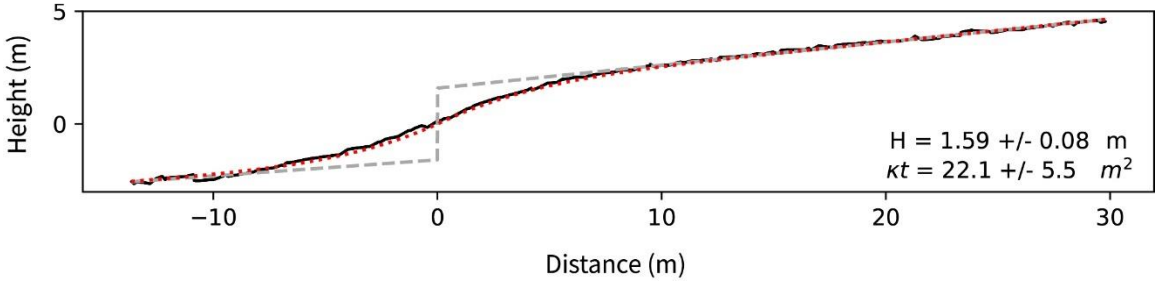

Figure 4-13. Extracted profile 12 from the location #1

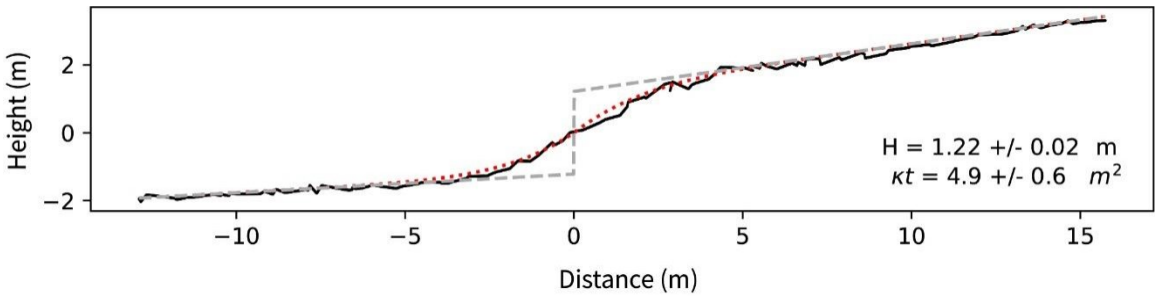

Figure 4-14. Extracted profile 22 from the location #2

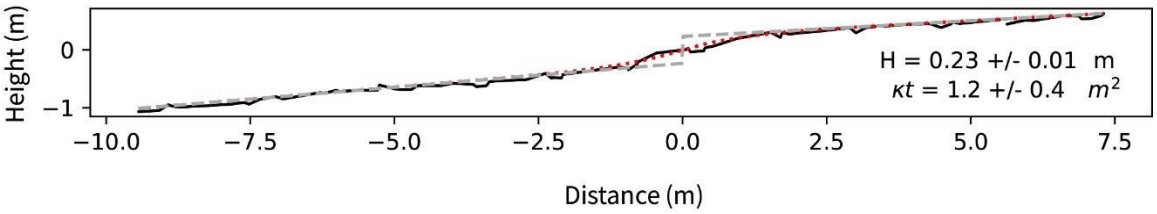

Figure 4-15. Extracted profile 32 from the location #3

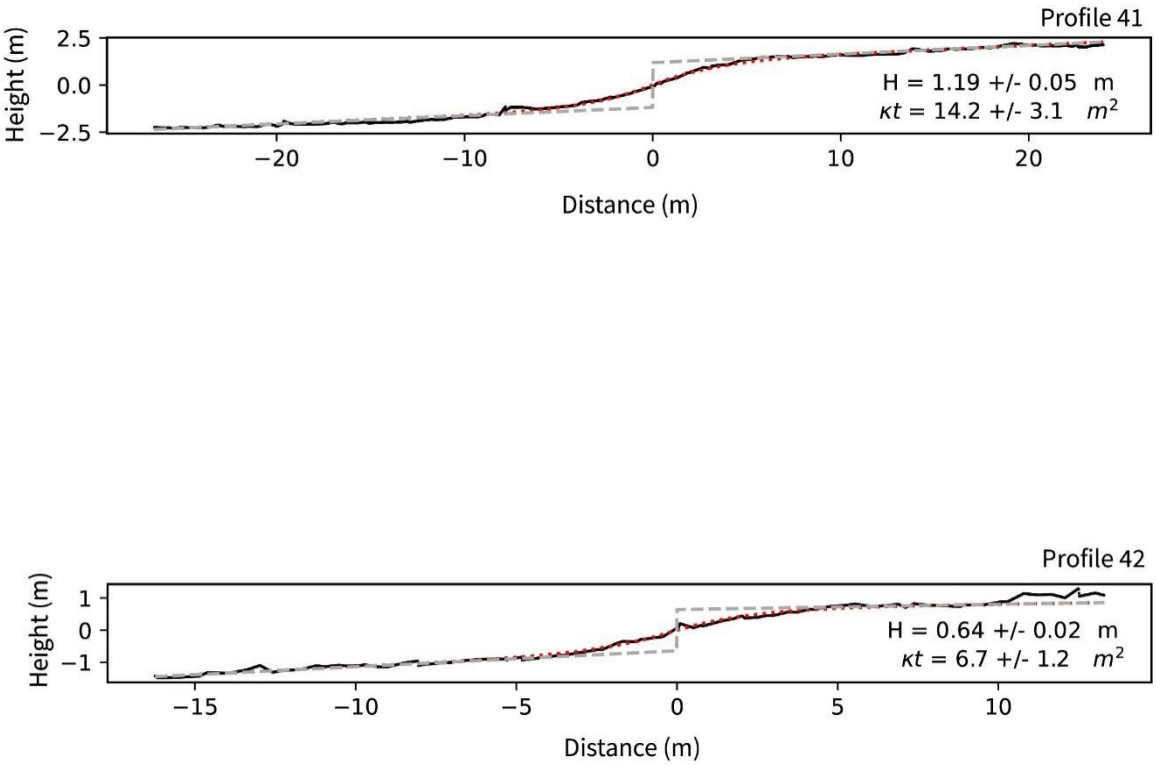

Figure 4-16. Extracted profiles 41 & 42 from the location #4

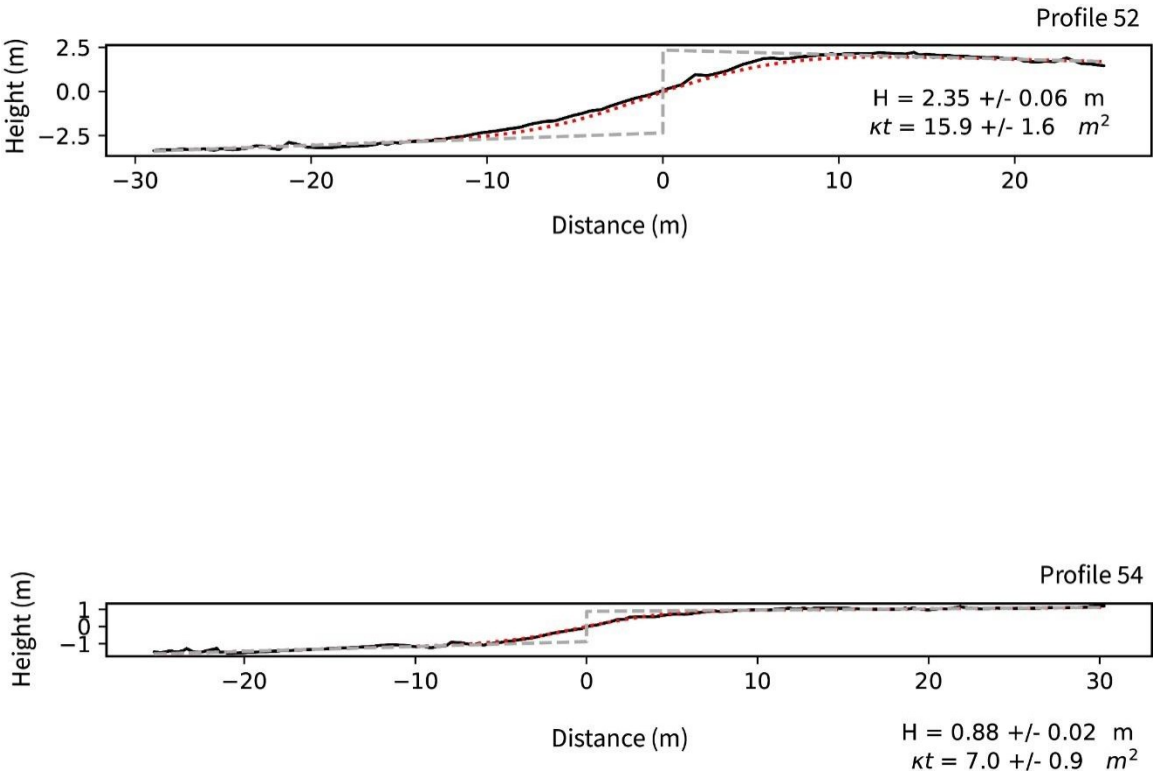

Figure 4-17. Extracted profiles 52 & 54 from the location #5

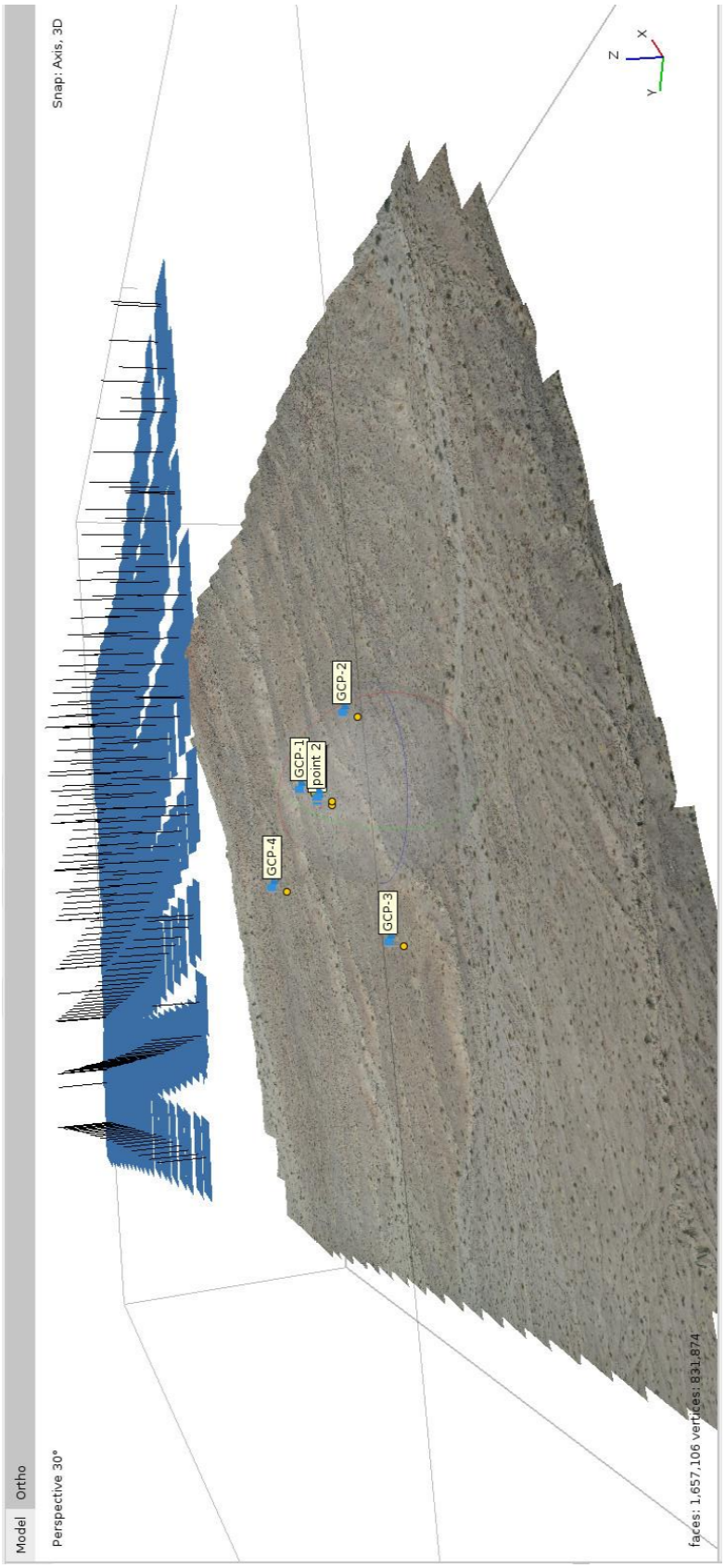

Figure 4-18. Photogrammetric point cloud, facing NE

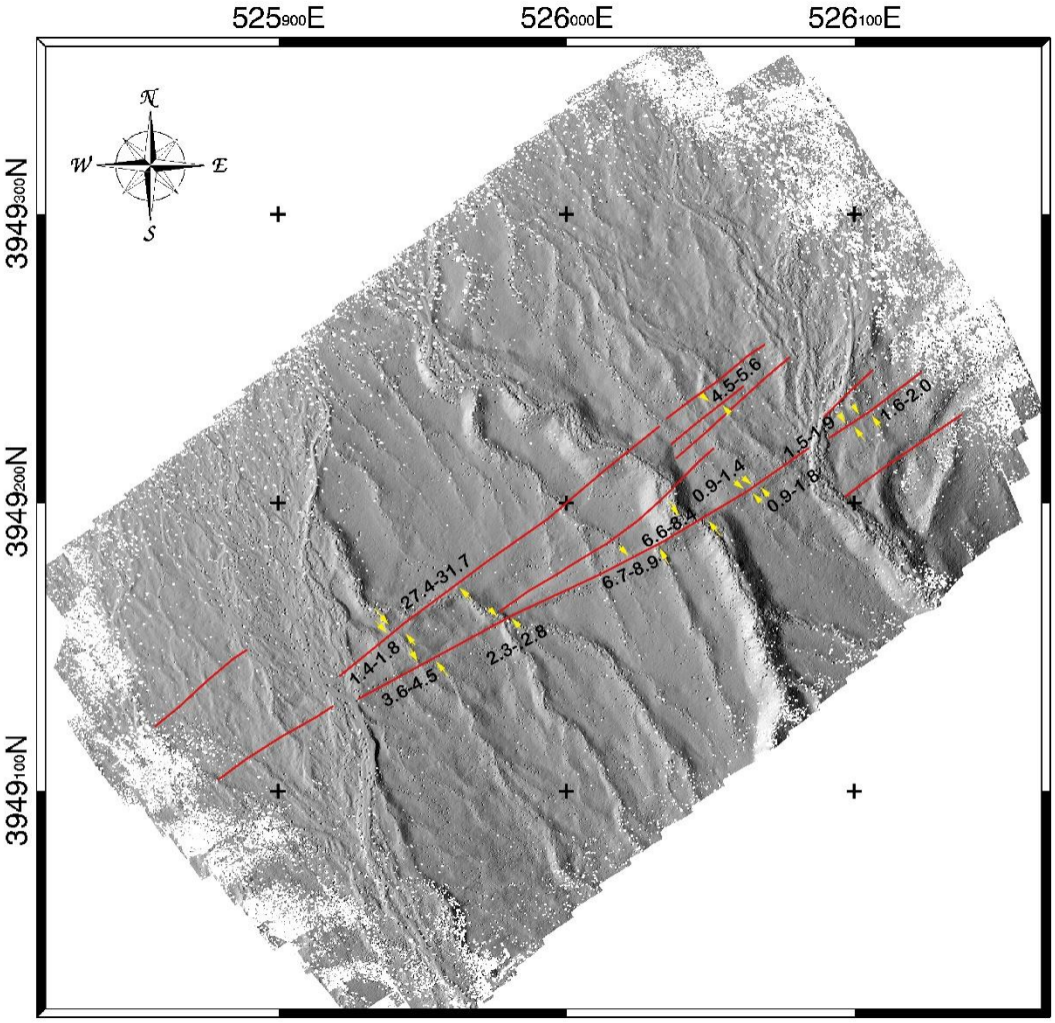

Figure 4-19. A shaded relief image of 4-cm-DEM. Faults are shown by the red lines. At the SW extent of the map, the fault is observed cutting through recent alluvium (Sun angle: Azimuth=90°, Elevation=40°). Measurements are in meters.

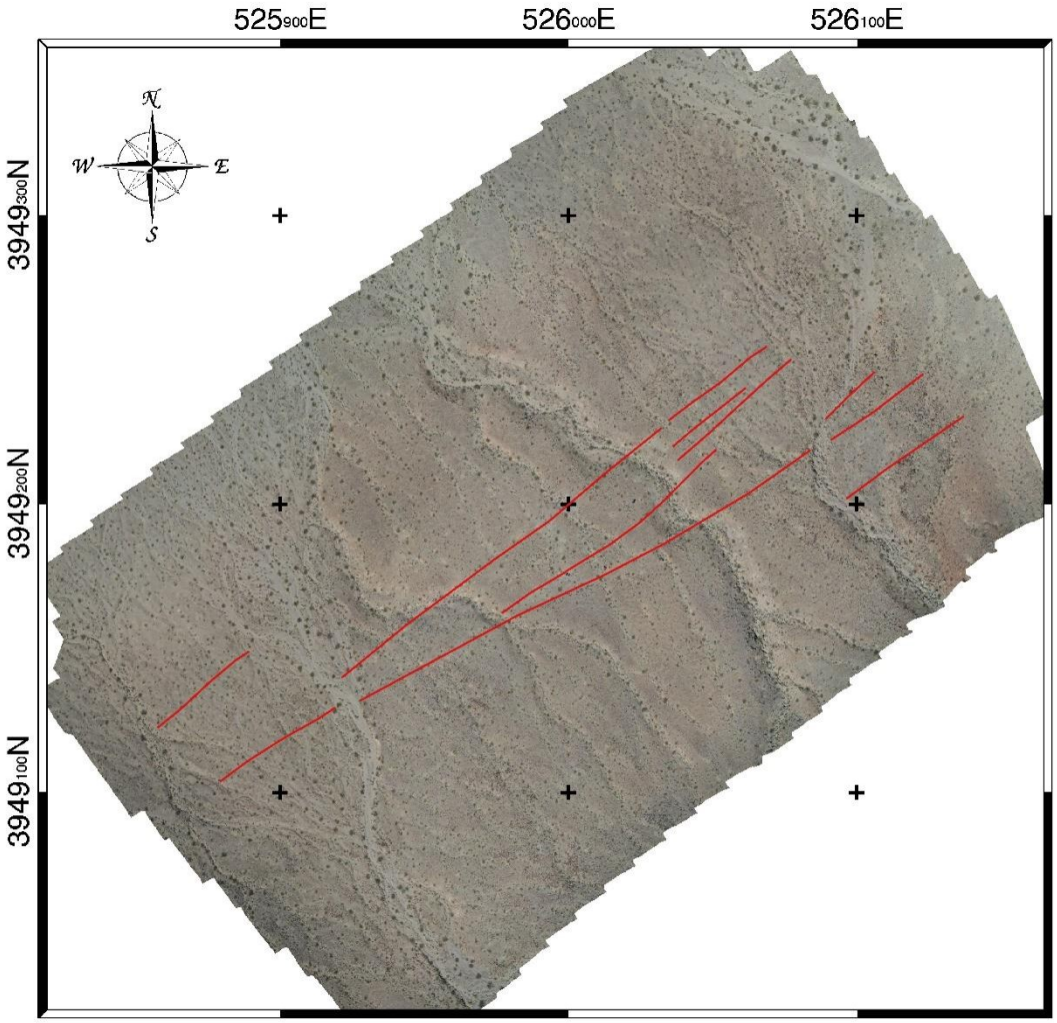

Figure 4-20. Owl Lake Fault - Orthophoto. Red lines: Main fault and its splays

5. DISCUSSION & CONCLUSION

Discussion

This neotectonic study provides a new estimate of the slip rate of the Owl Lake Fault, as well as an estimate of the smallest, single-earthquake displacement. These results can be used to reassess the hypotheses presented in Chapter 1.

This study found the slip rate of the Owl Lake Fault to be 1.1 -1.4 mm/yr this favors Hypothesis 1B (see chapter 1), which implies that some (most) of the slip from the Garlock Fault transfers eastward toward the Avawatz Mountains. It should be kept in mind that there are uncertainties owing to the methodology. One important consideration is the reliance on the mass diffusivity (κ) to estimate the age. Errors in κ will propagate proportionally into the slip rate; for example, if κ were doubled, the estimated slip rate would double. The estimate of the mass diffusivity constant κ determined in this study for Death Valley is comparable to other hyper-arid regions (e.g., the Dead Sea), but it is lower than estimates from the Basin and Range (1.1 m^2/kyr) (Hanks, 2000). This uncertainty can be addressed in future studies with better age constraints from more proximal locations – ideally along the Owl Lake Fault itself (see below). Additionally, the choice of scarp degradation model can influence the diffusion (and, consequently, the age) estimate. For fault scarps in the study area, the "steady-state" uplift model was applied, rather than the "single-event" model. Steady-state is an end-member case for a continuously creeping fault, and this could slightly over-estimate the age if the fault deviates from this assumption (Hanks et al., 1984).

Considering that the reported slip rates of the Central Garlock Fault range from 5.0 – 6.0 mm/yr (Ganev et al., 2012), the results of this study suggest that 3.9 - 4.6 mm/yr slip rate transfers eastward on the Garlock Fault (Figure 5-1). This is similar to the eastern Garlock Fault slip rate modeled by Zeng and Shen (2016) based on the GPS velocity. As discussed by Moore (2019), the horizontal shortening through the Avawatz Mountains is less than 0.5 mm/yr meaning the entire transferred slip rate does not contribute to the uplift of the Avawatz Mountains. This transferred slip rate may have an impact on the rotation of the Mojave block or may result to produce other structural elements (e.g., Guest et al., 2003).

The estimated slip rate of the Owl Lake Fault is in the lower range of that reported by McGill (1993), but as discussed previously, the age in that study may not be reliable. The new slip rate from this study (estimated over thousands of years) is lower than that modeled by Zeng and Shen (2016) based on regional GPS velocities (measured over 10 – 15 years). This discrepancy may result from transient deformations, such as accelerated post-seismic effects. However, the lack of a recent earthquake along the Owl Lake Fault suggests that is unlikely. Alternatively, the geodetic estimate may be poorly constrained by a paucity of survey sites near the Owl Lake Fault.

Concerning earthquake behavior (Hypotheses 2A and 2B), the smallest offset observed along the Owl Lake Fault was 1.6 ± 0.1 m, based on the low-altitude photogrammetric survey. The interpreted coseismic offset (1.6 ± 0.1 m) can be used to infer possible earthquake magnitudes using the empirical relationship between the average displacement (AD) and moment magnitude (M) by Wells and Coppersmith (1994) (Figure 5-2) for strike-slip faults:

$$M = 7.04 + 0.89 * \log(AD) \quad (8)$$

Using the average displacement (AD)=1.5 and 1.7 m, the observed offsets suggest a moment magnitude of approximately M=7.2 (Figure 5-3).

On the other hand, the length of the Owl Lake Fault is approximately 19-25 km. The moment magnitude also can be calculated with the empirical relationship between the surface rupture length (SRL) and moment magnitude (M) using the equation (9) (Wells and Coppersmith, 1994) (Figure 5-4) for strike-slip faults:

$$M = 5.16 + 1.12 * \log(SRL) \quad (9)$$

Using the rupture length (SRL) as a range from 19 km and 25 km, a moment magnitude M=6.6 to M=6.7 would be implied - this is discrepant with that suggested by the interpreted coseismic offset.

Average displacement (AD) and surface rupture length (SRL) also can be calculated with the empirical relationship between them by using the equation (10) (Wells and Coppersmith (1994) (Figure 5-5) for strike-slip faults:

$$\log(\mathrm{AD}) = -1.70 + 1.04 * \log(SRL) \quad (10)$$

Using the average displacement of 1.6 ± 0.1 m, surface rupture length is calculated as SRL=64 km and SRL=72 km, respectively. However, the length of the Owl Lake Fault is around 19-25 km. In order to sustain the observed coseismic offset (and associated magnitude), the Owl Lake Fault may need to rupture coseismically with part of central Garlock Fault (length=~107 km). These results lead to the prediction of Hypothesis 2B (see Chapter 1). Owing to fault geometry, the coseismic fault rupture probably involves

part of the central Garlock Fault. However, this does not seem to rupture the complete central Garlock Fault which begins at Koehn Lake, which begins more than 100 km west of the Owl Lake Fault.

It is important to remember that the photogrammetric survey was conducted on only one location along the fault. Also, an alternative interpretation of the offset would be as a maximum coseismic slip. Although this seems less likely, this would suggest a M=6.9 – 7.0 earthquake and a surface rupture length 40 – 45 km (i.e., still longer than the Owl Lake Fault) – this is still discrepant with the observed length of the Owl Lake Fault.

The average earthquake recurrence interval is calculated by dividing co-seismic displacement by the slip rate: $(1.6 \pm 0.1\ m) / (1.3 \pm 0.2\ mm/yr) = 1230 \pm 200$ years. There are no large, historical earthquakes on the Owl Lake Fault, and the fault currently lacks Paleoseismic studies. The central Garlock Fault has been studied at El Paso Peaks, approximately 80 km west of the Owl Lake Fault. At that location, 6 paleoseismic events during the past 7000-8000 year suggests a mean recurrence interval of 1100-1300 years, although there is very distinct temporal clustering (Dawson et al., 2003; Dolan et al., 2016).

Conclusions

Neotectonic investigations allowed to constrain the slip rate of the Owl Lake Fault as 1.1 - 1.4 mm/yr. The Owl Lake Fault can produce earthquake with the magnitude M=7.2 with the 1030 – 1430-yr recurrence interval. 3.9 - 4.6 mm/yr slip rate from the central Garlock Fault is transferred to the eastward to Avawatz Mountains and other structural complexes. This study suggest that the Owl Lake Fault is part of the same

hazard consideration as the central Garlock Fault. The possible rupture of the fault may include the part of the central Garlock Fault (from the intersection of the Garlock Fault and Owl Lake Fault to the El Paso Mountains). Since the region of the Owl Lake Fault is not populated, the risk of the potential future earthquake will be low.

In addition to the tectonic implications, this study also demonstrates that even if the available LiDAR data allows to map the fault and faulted landforms without field work, smallest offsets to determine possible single-event, coseismic displacements require higher resolution imaging (such as low-altitude photogrammetry used here).

Future Work

I aimed to use the Terrestrial Cosmogenic Nuclide (TCN) method for dating offset landforms for this study, especially ^{10}Be and ^{36}Cl. Dating these isotopes provide the age of the exposure time of the rocks and the ages of alluvial fans and other depositional surfaces. During the field work, eight bags of rock samples collected, but some of the samples were to small, so three bags were sent to the lab. Unfortunately, the dating results could not be obtained because of the dislocation. For future work, new samples can be collected to obtain dating results with TCN or other dating methods. These age results can be used to calibrate κ more precisely for other surfaces along the fault. Additionally, more low-altitude surveys can be conducted to identify the smallest offsets for accessible parts of the Owl Lake Fault. Besides, paleoseismic studies can be conducted in these areas to obtain the time of the last pre-historic earthquake.

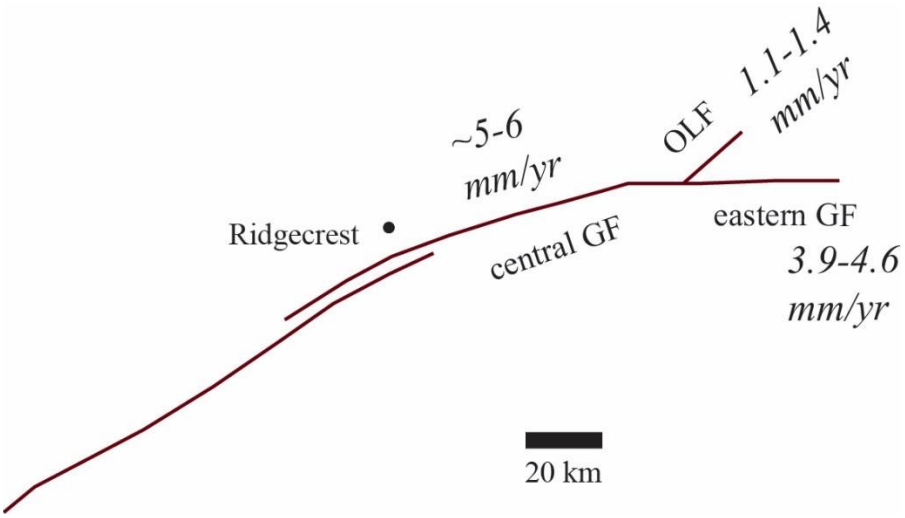

Figure 5-1. Illustration of slip transfer from the central Garlock Fault. OLF; Owl Lake Fault, GF; Garlock Fault

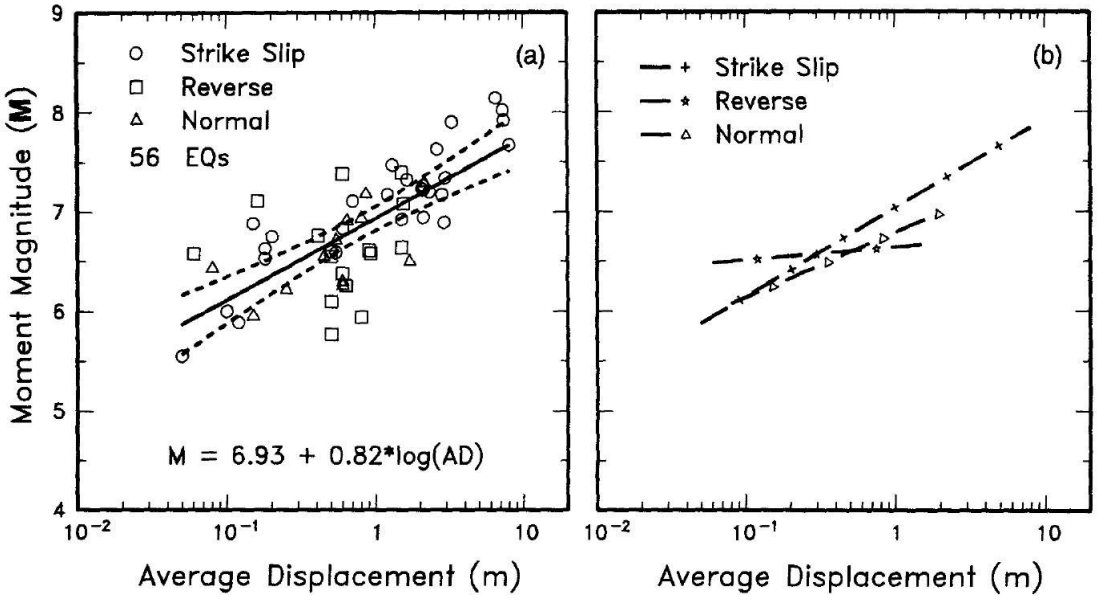

Figure 5-2. Log-linear regression and empirical relationship between average displacement and moment magnitude (Wells and Coppersmith, 1994)

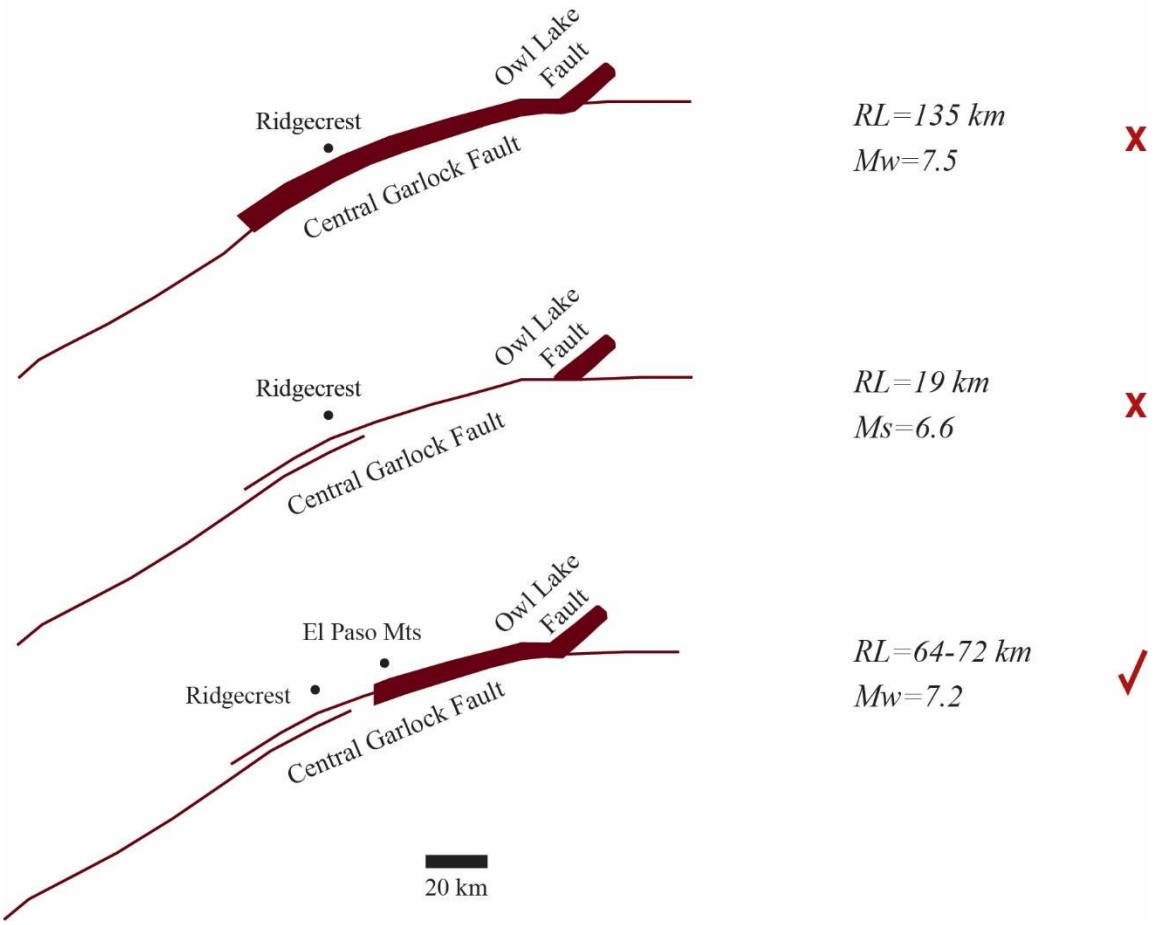

Figure 5-3. Possible rupture pattern for the Owl Lake Fault with previous studies. Modified from McGill and Sieh, 1991; McGill, 1992.

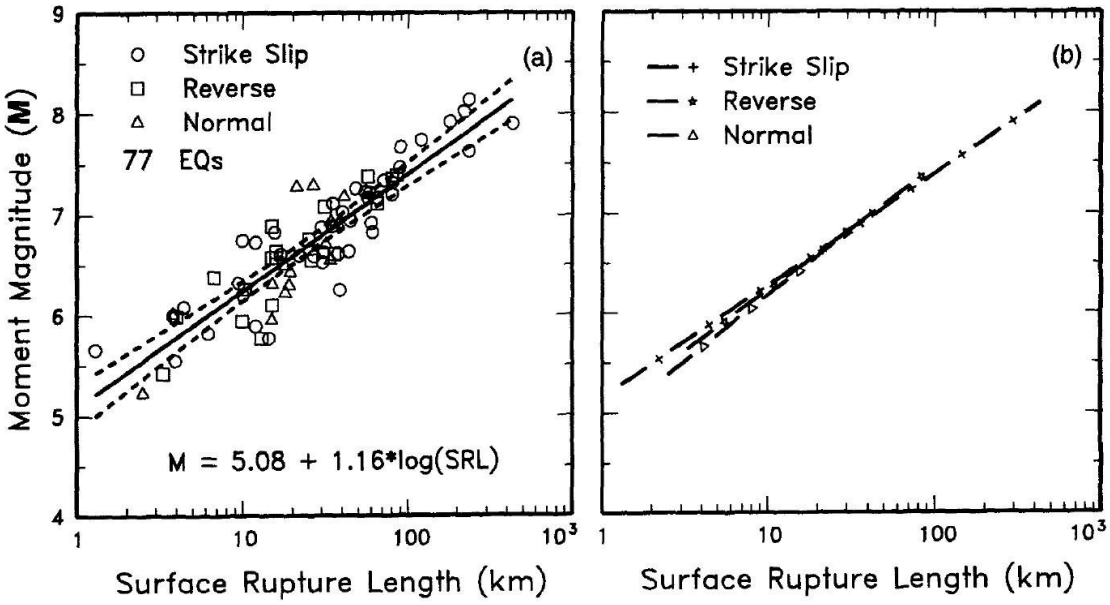

Figure 5-4. Log-linear regression and empirical relationship between surface rupture length and moment magnitude (Wells and Coppersmith, 1994)

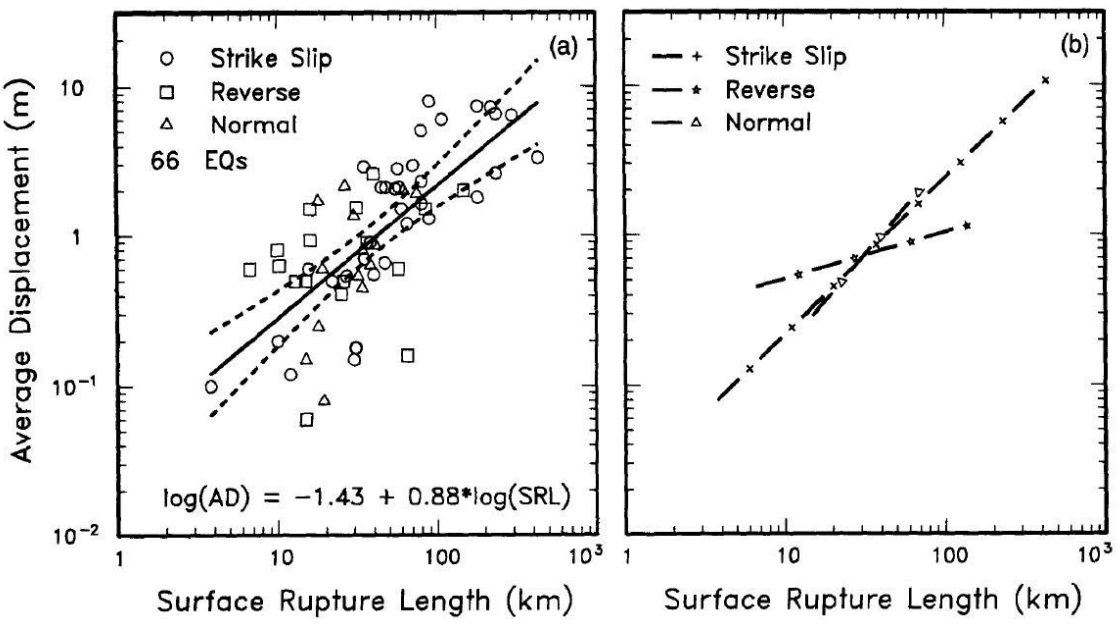

Figure 5-5. SRL Log-linear regression and empirical relationship between surface rupture length and average displacement (Wells and Coppersmith, 1994)

REFERENCES

Allen, C.R., 1975, Geological Criteria for Evaluating Seismicity, . Geological Society of America Bulletin, 86, 1041.

Andrew, J.E. and Walker, J.D., 2017, Path and Amount of Dextral Fault Slip in the Eastern California Shear Zone across the central Mojave Desert. GSA Bulletin, 129 (7-8): 855–868. doi: https://doi.org/10.1130/B31527.1.

Arrowsmith, J. R., Rhodes, D. D., and Pollard, D. D., 1998, Morphologic Dating of Scarps Formed by Repeated Slip Events along the San Andreas Fault, Carrizo Plain, California, Journal of Geophysical Research, 103(B5), 10141– 10160, doi:10.1029/98JB00505.

Astiz, L. and Allen, C.R., 1983, Seismicity of the Garlock Fault, California, Bulletin of the Seismological Society of America, 73 (6A): 1721–1734, doi: https://doi.org/10.1785/BSSA07306A1721.

Atwater, T.M., 1970, Implications of Plate Tectonics for the Cenozoic Evolution of western North America. Geological Society of America Bulletin, 81, 3513-3536. Geological Society of America Bulletin. 81. 10.1130/0016-7606(1970)81[3513:IOPTFT]2.0.CO;2.

Benedetti, L.C. and Van Der Woerd, J., 2014, Cosmogenic Nuclide Dating of Earthquakes, Faults, and Toppled Blocks, Elements, 10 (5): 357–361, doi: https://doi.org/10.2113/gselements.10.5.357.

Bennett, S.E.K., Oskin, M. E., Dorsey, R.J., Iriondo, A., and Kunk, M.J., 2015, Stratigraphy and Structural Development of the southwest Isla Tiburón Marine Basin: Implications for Latest Miocene Tectonic Opening and Flooding of the northern Gulf of California, Geosphere, 11 (4): 977–1007, doi: https://doi.org/10.1130/GES01153.1.

Bryant, W.A., 2003, Quaternary Fault and Fold Database of the United States: https://earthquake.usgs.gov/cfusion/qfault/show_reort_AB_archive.cfm?fault_id=69&section_id=c.

Burbank, D.W., and Whistler, D. P., 1987, Temporally Constrained Tectonic Rotations Derived from Magnetostratigraphic Data: Implications for the Initiation of the Garlock Fault, California: Geology, v. 15, p. 1172–1175, doi: https://doi.org/10.1130/0091-7613(1987)15<1172:TCTRDF>2.0.CO;2.

Camp, V.E., Pierce, K., and Morgan, L.A., 2015, Yellowstone Plume Trigger for Basin and Range Extension, and Coeval Emplacement of the Nevada--Columbia Basin Magmatic Belt, Geosphere, "First published on-line", doi:10.1130/GES01051.1.

Clark, M.M., 1973, Map Showing Recently Active Breaks along the Garlock and Associated Faults, California: U.S, Geological Survey, Miscellaneous Geological Investigations, Map, 1-741.

Davis, G.A. and Burchfiel, B.C., 1973, Garlock Fault: An Intracontinental Transform Structure, Southern California, Geological Society of America Bulletin, 84(4), 1407–1422, doi:10.1130/0016-7606(1973)84<1407:GFAITS>2.0.CO;2.

Dawson, T., McGill, S., and Rockwell, T., 2003, Irregular Recurrence of Paleoearthquakes along the central Garlock Fault near El Paso Peaks, California, Journal of Geophysical Research, 108, doi: 10.1029/2001JB001744.

Dickinson, W.R., and Wernicke, B.P., 1997, Reconciliation of San Andreas Slip Discrepancy by a Combination of Interior Basin and Range Extension and Transrotation near the Coast, Geology, 25 (7): 663–665, doi: https://doi.org/10.1130/0091-7613(1997)025<0663:ROSASD>2.3.CO;2.

Dixon, T.H. and Xie, S., 2018, A kinematic model for the evolution of the Eastern California Shear Zone and Garlock Fault, Mojave Desert, California, Earth and Planetary Science Letters, Volume 494, Pages 60-68, ISSN 0012-821X, https://doi.org/10.1016/j.epsl.2018.04.050.

Dokka, R.K. and Travis, C.J., 1990a, Late Cenozoic strike-slip faulting in the Mojave Desert, California: Tectonics, v. 9, p. 311-340, doi:10.1029/TC009i002p00311.

Dokka, R.K. and Travis, C.J., 1990b, Role of the eastern California shear zone in accommodating Pacific–North American plate motion, Geophysics Research Letters, 17 (9), 1323–1326, https://doi .org /10 .1029 /GL017i009p01323.

Dolan, J.F., McAuliffe, L.J., Rhodes, E.J., McGill, S.F., and Zinke, R., 2016, Extreme Multi-millennial Slip Rate Variations on the Garlock Fault, California: Strain Super-cycles, Potentially Time-variable Fault Strength, and Implications for System-level Earthquake Occurrence, Earth and Planetary Science Letters, Volume 446, 123-136, https://doi.org/10.1016/j.epsl.2016.04.011.

Dorn, R.I., 1996, Letters to The Editor: Uncertainties In The Radiocarbon Dating Of Organics Associated With Rock Varnish: A Plea For Caution, Physical Geography, 17:6, 585-591, doi: 10.1080/02723646.1996.10642602.

Drury, S.A., 2004, Image Interpretation in Geology, 3rd Edition, Malden, MA, Blackwell Science, 304p.

Fonstad, M.A., Dietrich, J.T., Courville, B.C., Jensen, J.L. and Carbonneau, P.E., 2013, Topographic Structure from Motion: A New Development in Photogrammetric

Measurement. Earth Surface Processes and Landforms, 38: 421-430, https://doi.org/10.1002/esp.3366.

Frankel, K.L., Lee, J., Bishop, K., Dawers, N., Ganev, P., Unruh, J., and Owen, L.A., 2010, Miocene - Quaternary Tectonic Evolution of the Northern Eastern California Shear Zone, in Clifton, H.E., and Ingersoll, R.V., eds., Geologic Excursions in California and Nevada: Tectonics, Stratigraphy and Hydrogeology: Pacific Section, SEPM (Society for Sedimentary Geology) Book 108, p. 173-231.

Frankel, K.L., Owen, L.A., Dolan, J.F., Knott, J.R., Lifton, Z.M., Finkel, R.C., and Wasklewicz, T., 2015, Timing and Rates of Holocene Normal Faulting along the Black Mountains Fault Zone, Death Valley, USA, Lithosphere, 8 (1): 3–22, doi: https://doi.org/10.1130/L464.1.

Ganev, P. N., Dolan, J. F., McGill, S. F., and Frankel, K. L., 2012, Constancy of Geologic Slip Rate along the central Garlock Fault: Implications for Strain Accumulation and Release in southern California: Geophysical Journal International, 190(2), 745-760, https://doi.org/10.1111/j.1365-246X.2012.05494.x.

Geyh, M.A. and Schleicher, H., 1990, Absolute Age Determination: Physical and Chemical Dating Methods and Their Application, Mineralogical Magazine, 55(380), 487-488, doi:10.1180/minmag.1991.055.380.19.

Golombek, M.P. and Brown, L.L., 1988, Clockwise Rotation of the western Mojave Desert, Geology, 16(2), 126–130, doi:10.1130/0091-7613(1988)016<0126:CROTWM>2.3.CO;2.

Gourmelen, N., Dixon, T.H., Amelung, F., and Schmalzle, G., 2011, Acceleration and Evolution of Faults: An Example from the Hunter Mountain – Panamint Valley Fault Zone, Eastern California, Earth and Planetary Science Letters, Volume 301, Issues 1–2, Pages 337-344, ISSN 0012-821X, https://doi.org/10.1016/j.epsl.2010.11.016.

Guest, B., Pavlis, T. L., Golding, H., and Serpa, L., 2003, Chasing the Garlock: A study of tectonic response to vertical axis rotation. Geology, 31(6), 553. doi:10.1130/0091-7613(2003)031<0553:ctgaso>2.0.co;2.

Hanks, T.C., 2000, The Age of Scarplike Landforms from Diffusion-Equation Analysis, In Quaternary Geochronology (eds J.S. Noller, J.M. Sowers and W.R. Lettis), https://doi.org/10.1029/RF004p0313.

Hanks, T. C., Bucknam, R. C., Lajoie, K. R., and Wallace, R. E., 1984, Modification of Wave-Cut and Faulting-Controlled Landforms: Journal of Geophysical Research, v . 89, p. 5771-5790, https://doi.org/10.1029/JB089iB07p05771.

Keller, E.A. and Pinter, N., 2002, Active Tectonics, Earthquakes, Uplift and Landscape, 2nd Edition, Prentice Hall, Upper Saddle River, 362 p.

Liu, M., Wang, H., and Q. Li, 2010, Inception of the eastern California Shear Zone and Evolution of the Pacific-North American Plate Boundary: From Kinematics to Geodynamics, Journal of Geophysical Research, 115, B07401, doi:10.1029/2009JB007055.

McGill, S.F., 1993, Late Quaternary Slip Rate of the Owl Lake Fault and Maximum Age of the Latest Event on the easternmost Garlock Fault, S. California: Geological Society of America Abstracts with Programs, v. 25, no. 5, p. 118.

McGill, S.F., 1998a, Preliminary slip-rate estimate for the Owl Lake Fault, California, in Calzia, J.P., and Reynolds, R.E., eds., Finding Faults in the Mojave: San Bernardino County Museum Association Quarterly, v. 45, p. 84-87.

McGill, S.F., 1998b, Summary of Neotectonic Slip-Rate Studies of the Garlock and Owl Lake Fault Zones, in Calzia, J.P., and Reynolds, R.E., eds., Finding Faults in the Mojave: San Bernardino County Museum Association Quarterly, v. 45, p. 88-90.

McGill, S.F., 1999, Slip-rate studies of the Garlock and Owl Lake Faults: U.S. Geological Survey National Earthquake Hazards Reduction Program, Annual Summaries v. 40, Contract no. 1434-92-G-2210, 6 p., (electronic version online at http://erp-web.er.usgs.gov/).

McGill, S.F. and Sieh, K., 1991, Surficial offsets on the central and eastern Garlock Fault associated with prehistoric earthquakes: C, v. 96, p. 21,587-21,621.

McGill, S.F. and Sieh, K., 1993, Holocene Slip Rate of the Central Garlock Fault in southeastern Searles Valley, California, Journal of Geophysical Research, 98(B8), 14217–14231, doi:10.1029/93jb00442.

McGill, S.H.F., 1992, Paleoseismology and Neotectonics of the central and eastern Garlock Fault, California: Pasadena, California Institute of Technology, unpublished Ph.D. dissertation, 235 p.

Miller, B.D.M., Menges, C.M., and Lidke, D.J., 2014, Generalized Surficial Geologic Map of the Fort Irwin Area, San Bernardino County, California: Geology and Geophysics Applied to Groundwater Hydrology at Fort Irwin, California, p. 1–11.

Monastero, F.C., Sabin, A.E. & Walker, J.D., 1997, Evidence for Past-early Miocene Initiation of Movement on the Garlock Fault from Offset of the Cudahy Camp Formation, east-central California, Geology, 25, 247–250, doi:10.1130/0091-7613(1997)025<0247:EFPEMI>2.3.CO;2.

Moore, K., 2019, Neotectonic and Geophysical Investigation into the Active Growth of the Avawatz Mountain Front, California, Master's Thesis, University of Missouri – Columbia.

Muehlberger, W.R., 1954, Geology of the Quail Mountains, San Bernardino County: California Division of Mines Bulletin 170, Geology of Southern California Map Sheet 16, scale 1:48,000.

Oskin, M., and J. Stock, 2003, Pacific-North America Plate Motion and Opening of the Upper Delfin Basin, northern Gulf of California, Mexico, Geological Society of America Bulletin, 115(10), 1173–1190.

Parsons, T., 2006, Chapter 7, The Basin and Range Province, Developments in Geotectonics, 25, doi:10.1016/S0419-0254(06)80015-7.

Petersen, M.D. and Wesnousky, S.G., 1994, Fault Slip Rates and Earthquake Histories for Active Faults in southern California. Bulletin of the Seismological Society of America, 84 (5): 1608–1649, doi: https://doi.org/10.1785/BSSA0840051608.

Plattner, C., Malservisi, R., Furlong, K.P., and Govers, R., 2010, Development of the Eastern California Shear Zone - Walker Lane Belt: The Effects of Microplate Motion and Pre-existing Weakness in the Basin and Range, Tectonophysics, Volume 485, Issues 1–4, Pages 78-84, ISSN 0040-1951, doi:10.1016/j.tecto.2009.11.021.

Plescia, J.B. and Henyey, T. L., 1982, Geophysical Character of the Proposed eastern Extension of the Garlock Fault and Adjacent Areas, eastern California, Geology, 10 (4), 209–214, doi:10.1130/0091-7613(1982)10<209:GCOTPE>2.0.CO;2.

Polun, S., Bidgoli, T., and Gomez, F., 2021, Developing an Integrated Surface-Age — Remote Sensing Spectral Property Model to Enable Slip Rate Studies in Inaccessible Regions: Examples and Challenges from the Mojave Desert, AGU Fall Meeting, New Orleans, LA.

Rittase, W.M., Kirby, E., McDonald, E., Walker, J.D., Gosse, J., Spencer, J.Q.G., and Herrs, A.J., 2014, Temporal Variations in Holocene Slip Rate along the central Garlock Fault, Pilot Knob Valley, California, Lithosphere, 6 (1): 48–58, doi: https://doi.org/10.1130/L286.1.

Schermer, E. R., Luyendyk, B. P., and Cisowski, S., 1996, Late Cenozoic Structure and Tectonics of the northern Mojave Desert, Tectonics, 15(5), 905– 932, doi:10.1029/96TC00131.

Wernicke, B., 1992, Cenozoic Extensional Tectonics of the U.S. Cordillera, in Burchfiel, B.C., Lipman, P.W., and Zoback, M.L., eds., The Cordilleran Orogen:

Conterminous U.S.: Boulder, Colorado, Geological Society of America, The Geology of North America, v. G-3, https://doi.org/10.1130/DNAG-GNA-G3.553.

Wells, D. L., Coppersmith, K. J., 1994, New Empirical Relationships among Magnitude, Rupture Length, Rupture Width, Rupture Area, and Surface Displacement, Bulletin of the Seismological Society of America, 84(4), 974-1002.

Wesson, R.L., Helley, E.J., Lajoie, K.R., and Wentworth, C.M., 1975, Faults and Future Earthquakes, in Borcherdt, R.D., ed., Studies for Seismic Zonation of the San Francisco Bay Region: U.S. Geological Survey Professional Paper 941-A, p. A5–A30.

Yeats, R.S., Sieh, K., and Allen, C.R., 1996, The Geology of Earthquakes, Oxford University Press, Oxford. 568p.

Zeng, Y. and Shen, Z.K., 2016, A Fault-Based Model for Crustal Deformation, Fault Slip Rates, and Off-Fault Strain Rate in California, Bulletin of the Seismological Society of America, doi:106. 10.1785/0120140250.